



AFRL-RB-WP-TR-2008-3055

NUMERICAL STUDY OF ACTIVE FLOW CONTROL FOR A TRANSITIONAL HIGHLY-LOADED LOW-PRESSURE TURBINE

Donald P. Rizzetta and Miguel R. Visbal

**Computational Sciences Branch
Aeronautical Sciences Division**

**FEBRUARY 2008
Final Report**

Approved for public release; distribution unlimited.

See additional restrictions described on inside pages

STINFO COPY

**AIR FORCE RESEARCH LABORATORY
AIR VEHICLES DIRECTORATE
WRIGHT-PATTERSON AIR FORCE BASE, OH 45433-7542
AIR FORCE MATERIEL COMMAND
UNITED STATES AIR FORCE**

NOTICE AND SIGNATURE PAGE

Using Government drawings, specifications, or other data included in this document for any purpose other than Government procurement does not in any way obligate the U.S. Government. The fact that the Government formulated or supplied the drawings, specifications, or other data does not license the holder or any other person or corporation; or convey any rights or permission to manufacture, use, or sell any patented invention that may relate to them.

This report was cleared for public release by the Air Force Research Laboratory Wright Site (AFRL/WS) Public Affairs Office and is available to the general public, including foreign nationals. Copies may be obtained from the Defense Technical Information Center (DTIC) (<http://www.dtic.mil>).

AFRL-RB-WP-TR-2008-3055 HAS BEEN REVIEWED AND IS APPROVED FOR PUBLICATION IN ACCORDANCE WITH ASSIGNED DISTRIBUTION STATEMENT.

*//Signature//

MIGUEL R. VISBAL, Technical Area Leader
Computational Sciences Branch
Aeronautical Sciences Division

//Signature//

REID B. MELVILLE, Chief
Computational Sciences Branch
Aeronautical Sciences Division

//Signature//

MATTHEW BURKINSHAW, Technical Advisor
Computational Sciences Branch
Aeronautical Sciences Division

This report is published in the interest of scientific and technical information exchange, and its publication does not constitute the Government's approval or disapproval of its ideas or findings.

*Disseminated copies will show “//Signature//” stamped or typed above the signature blocks.

REPORT DOCUMENTATION PAGE				<i>Form Approved</i> OMB No. 0704-0188	
The public reporting burden for this collection of information is estimated to average 1 hour per response, including the time for reviewing instructions, searching existing data sources, gathering and maintaining the data needed, and completing and reviewing the collection of information. Send comments regarding this burden estimate or any other aspect of this collection of information, including suggestions for reducing this burden, to Department of Defense, Washington Headquarters Services, Directorate for Information Operations and Reports (0704-0188), 1215 Jefferson Davis Highway, Suite 1204, Arlington, VA 22202-4302. Respondents should be aware that notwithstanding any other provision of law, no person shall be subject to any penalty for failing to comply with a collection of information if it does not display a currently valid OMB control number. PLEASE DO NOT RETURN YOUR FORM TO THE ABOVE ADDRESS.					
1. REPORT DATE (DD-MM-YY) February 2008		2. REPORT TYPE Final		3. DATES COVERED (From - To) 01 June 2002 – 30 January 2007	
4. TITLE AND SUBTITLE NUMERICAL STUDY OF ACTIVE FLOW CONTROL FOR A TRANSITIONAL HIGHLY-LOADED LOW-PRESSURE TURBINE				5a. CONTRACT NUMBER In-house	
				5b. GRANT NUMBER	
				5c. PROGRAM ELEMENT NUMBER 0601102	
6. AUTHOR(S) Donald P. Rizzetta and Miguel R. Visbal				5d. PROJECT NUMBER A04Y	
				5e. TASK NUMBER	
				5f. WORK UNIT NUMBER 0C	
7. PERFORMING ORGANIZATION NAME(S) AND ADDRESS(ES) Computational Sciences Branch (AFRL/RBAC) Aeronautical Sciences Division Air Force Research Laboratory, Air Vehicles Directorate Wright-Patterson Air Force Base, OH 45433-7542 Air Force Materiel Command, United States Air Force				8. PERFORMING ORGANIZATION REPORT NUMBER AFRL-RB-WP-TR-2008-3055	
9. SPONSORING/MONITORING AGENCY NAME(S) AND ADDRESS(ES) Air Force Research Laboratory Air Vehicles Directorate Wright-Patterson Air Force Base, OH 45433-7542 Air Force Materiel Command United States Air Force				10. SPONSORING/MONITORING AGENCY ACRONYM(S) AFRL/RBAC	
				11. SPONSORING/MONITORING AGENCY REPORT NUMBER(S) AFRL-RB-WP-TR-2008-3055	
12. DISTRIBUTION/AVAILABILITY STATEMENT Approved for public release; distribution unlimited.					
13. SUPPLEMENTARY NOTES PAO Case Number: AFRL/WS 05-0752, 06 April 2005. Report contains color.					
14. ABSTRACT <p>Active control was simulated numerically for subsonic flow through a highly-loaded low-pressure turbine. At a nominal Reynolds number of 25,000 based upon axial chord and inlet conditions, massive separation occurred on the suction surface of each blade. Vortex generating jets were then used to help mitigate separation, thereby reducing wake losses. Computations were performed using both steady blowing and pulsed mass injections. The numerical method utilized a centered compact finite-difference scheme to represent spatial derivatives in conjunction with a low-pass Pade-type non-dispersive filter operator to maintain stability. Calculations were carried out on a massively parallel computing platform, using domain decomposition and a high-order overset grid approach.</p> <p>Features of the flow fields are described, and simulations are compared with each other, with available experimental data, and with a previously obtained baseline case for the non-controlled flow. Active flow control resulted in a reduction of the wake total pressure loss coefficient of 53-56%.</p>					
15. SUBJECT TERMS Active flow control, low-pressure turbine, turbulence simulation					
16. SECURITY CLASSIFICATION OF:			17. LIMITATION OF ABSTRACT: SAR	18. NUMBER OF PAGES 50	19a. NAME OF RESPONSIBLE PERSON (Monitor) Miguel R. Visbal 19b. TELEPHONE NUMBER (Include Area Code) N/A
a. REPORT Unclassified	b. ABSTRACT Unclassified	c. THIS PAGE Unclassified			

Table of Contents

List of Figures	iv
List of Tables	iv
Acknowledgements	v
1 Introduction	1
2 The Governing Equations	3
3 The Numerical Method	4
4 Details of the Computations	5
4.1 Computational Meshes	5
4.2 Temporal Considerations	6
4.3 Boundary Conditions	6
4.4 Domain Decomposition	7
5 Results	8
5.1 The Time-Mean Flowfields	8
5.2 Unsteady Features of the Flowfields	9
6 Summary and Conclusion	11
7 References	36
List of Symbols	39

List of Figures

1	Schematic representation of the turbine blade configuration.	12
2	Vortex generator jet geometry.	13
3	Turbine blade computational mesh.	14
4	Refined-mesh region.	15
5	Vortex-generator jet region.	16
6	Upstream and downstream computational meshes.	17
7	Jet blowing ratio time history.	18
8	Time-mean surface pressure coefficient distributions.	19
9	Time-mean velocity magnitude profiles at upstream stations.	20
10	Time-mean velocity magnitude profiles at downstream stations.	21
11	Time-mean turbulent kinetic energy spanwise wave-number spectra.	22
12	Time-mean planar contours of u velocity.	23
13	Time-mean contours of the spanwise component of vorticity.	24
14	Time-mean contours of the spanwise component of vorticity on the blade surface.	25
15	Time-mean fluctuating velocity magnitude profiles.	26
16	Turbulent kinetic energy frequency spectra.	27
17	Instantaneous planar contours of u velocity.	28
18	Instantaneous planar contours of the spanwise component of vorticity.	29
19	Instantaneous iso-surfaces of vorticity magnitude in the trailing-edge region.	30
20	Instantaneous planar contours of the spanwise component of vorticity on the blade surface.	31
21	Instantaneous iso-surfaces of vorticity magnitude in the near-jet region.	32
22	Instantaneous planar contours of the streamwise component of vorticity for the steady injection case.	33
23	Instantaneous planar contours of the streamwise component of vorticity for the pulsed injection case at $t/t_p = 0.5$	34
24	Instantaneous planar contours of the streamwise component of vorticity for the pulsed injection case at $t/t_p = 1.0$	35

List of Tables

1	Computational mesh spacings in wall units.	6
---	--	---

Acknowledgements

All of the work reported here was sponsored by the U. S. Air Force Office of Scientific Research. Computational resources were supported in part by grants of supercomputer time from the U. S. Department of Defense Major Shared Resource Centers at Wright-Patterson AFB, OH, Vicksburg, MS, Stennis Space Center, MS, and Aberdeen Proving Ground, MD. The authors are grateful to R. Sondergaard for supplying experimental results.

1 Introduction

Uninhabited air vehicles (UAVs) employed for reconnaissance and combat missions commonly utilize low-pressure turbines in their propulsion systems. Due to a reduction in atmospheric density during high-altitude cruise, such low-pressure turbines may encounter Reynolds numbers, based upon blade axial chord and inlet conditions, below 25,000. In this situation, boundary layers along a large extent of blade surfaces can remain laminar, even in the presence of elevated freestream turbulence levels. The laminar boundary layers are then particularly susceptible to flow separation over the aft portion of blade suction surfaces, causing blockage in flow passages and a significant reduction in turbine efficiency. These circumstances may thus result in imposed ceiling limitations for prolonged UAV deployment.

A number of experimental studies [1, 2, 3, 4, 5, 6, 7, 8] have identified several factors contributing to performance degradation in low-pressure turbines, which in addition to the Reynolds number include freestream turbulence, pressure gradient, and curvature. Because of the impact upon UAV operations, a number of experiments have focused on flow control as a means of reducing efficiency degradation at altitude. It was found by Lake et al.[9] that boundary-layer separation could be mitigated by modifying the turbine blade geometry. Dimples were recessed into blade suction surfaces in order to maintain the region of attached flow. Although this passive technique increases efficiency at low-Reynolds numbers, it may also increase viscous losses at higher Reynolds numbers such as those that occur during takeoff, where unmodified blades perform satisfactorily.

As an alternative, Bons et al. [10, 11, 12] and Sondergaard et al.[13] have explored active flow control in the form of both steady and pulsed vortex generator jets, which may be actuated upon demand. Extensive measurements verified that the jets dramatically reduced separation, resulting in decreased losses. Plasma control has also been demonstrated by Huang et al.[14] to restrict separation. More recent experiments by Sondergaard et al., [15] have investigated the feasibility of increasing the blade spacing at constant chord for a linear low-pressure turbine cascade, thereby raising the per blade loading. For practical applications, a higher loading can reduce the turbine part count and stage weight. Increased blade spacing however, is accompanied by more extensive boundary-layer separation on the suction surface of each blade due to uncovered turning, resulting in a further reduction of efficiency and additional wake losses. Vortex generator jets were then employed to diminish these losses by maintaining attached boundary-layer flow over a greater distance along the blade surface.

Numerical computations of low-pressure turbines have traditionally been predicated on solution of the Reynolds-averaged Navier-Stokes (RANS) equations. [16, 17, 18, 19, 20] Although these efforts have been moderately successful in predicting some of the overall features of the turbine flowfields, limitations and deficiencies of RANS turbulence models have precluded an accurate description of low-Reynolds separation and the transition to turbulence. Moreover, it is unlikely that the RANS approach will be adequate for simulating active flow control applications in the transitional regime.

Due to advances in the speed and storage capacity of high-performance computing systems, direct numerical simulation (DNS) and large-eddy simulation (LES) have emerged as viable means for the investigation of flows through low-pressure turbines. [21, 22, 23, 24, 25, 26, 27, 28] DNS and LES supported by high-order numerical methods improve predictive capability where RANS models fail, and allow for the simulation of flow control strategies. Several previous computations [23, 24, 27, 28] have been related to the experiments of Bons et al., [10, 11, 12] Sondergaard et al.,[15, 13] and Rivir et al.[29] In particular, the calculations of Rizzetta and Visbal [27] considered the highly-loaded low-pressure turbine configuration investigated by Sondergaard et al. [15] Simulations were carried out for both an uncontrolled baseline case, and a case with active flow control in the form of pulsed vortex generating jets. Although the aft-blade separation was mitigated and wake total pressure losses were decreased by the use of pulsed injection, the jet momentum coefficient employed in the computation was appreciably lower than that of the experiment. Consequently, the amount of control attained by the simulation was less substantial than that observed by Sondergaard et al. [15]

Control of the highly-loaded low-pressure turbine considered by Sondergaard et al. [15] consisted only of steady vortex generator jets. And while prior investigations verified that separation could be similarly managed by pulsed injection, [11, 12] it is unclear how the detailed behavior of the individual flow control arrangements differs. The purpose of the present work was to conduct numerical computations of the turbine configuration which approximate the experiment of Sondergaard et al. [15] Steady vortex generator jet flow

control matching the experimental jet momentum coefficient was simulated at a chord inlet Reynolds number of approximately 25,000. In addition, a calculation was also performed for pulsed jet injection, with a duty cycle that was one half that of the steady case. This allows for a direct comparison between the respective flow control situations, as well as with the baseline case, so that characteristics of the flowfields may be elucidated.

2 The Governing Equations

The governing equations are taken as the unsteady three-dimensional compressible unfiltered Navier-Stokes equations. After introducing a curvilinear coordinate transformation to a body-fitted system, the equations are cast in the following nondimensional conservative form

$$\frac{\partial}{\partial t} \left(\frac{Q}{J} \right) + \frac{\partial}{\partial \xi} \left(F - \frac{1}{Re_\infty} F_v \right) + \frac{\partial}{\partial \eta} \left(G - \frac{1}{Re_\infty} G_v \right) + \frac{\partial}{\partial \zeta} \left(H - \frac{1}{Re_\infty} H_v \right) = 0. \quad (1)$$

Here t is the time, ξ, η, ζ the computational coordinates, Q the vector of dependent variables, F, G, H the inviscid flux vectors, and F_v, G_v, H_v the viscous flux vectors. The vector of dependent variables is given as

$$Q = \begin{bmatrix} \rho & \rho u & \rho v & \rho w & \rho E \end{bmatrix}^T \quad (2)$$

and the vector fluxes by

$$F = \frac{1}{J} \begin{bmatrix} \rho U \\ \rho u U + \xi_x p \\ \rho v U + \xi_y p \\ \rho w U + \xi_z p \\ \rho E U + \xi_{x_i} u_i p \end{bmatrix}, \quad G = \frac{1}{J} \begin{bmatrix} \rho V \\ \rho u V + \eta_x p \\ \rho v V + \eta_y p \\ \rho w V + \eta_z p \\ \rho E V + \eta_{x_i} u_i p \end{bmatrix}, \quad H = \frac{1}{J} \begin{bmatrix} \rho W \\ \rho u W + \zeta_x p \\ \rho v W + \zeta_y p \\ \rho w W + \zeta_z p \\ \rho E W + \zeta_{x_i} u_i p \end{bmatrix} \quad (3)$$

$$F_v = \frac{1}{J} \begin{bmatrix} 0 \\ \xi_{x_i} \tau_{i1} \\ \xi_{x_i} \tau_{i2} \\ \xi_{x_i} \tau_{i3} \\ \xi_{x_i} (u_j \tau_{ij} - Q_i) \end{bmatrix}, \quad G_v = \frac{1}{J} \begin{bmatrix} 0 \\ \eta_{x_i} \tau_{i1} \\ \eta_{x_i} \tau_{i2} \\ \eta_{x_i} \tau_{i3} \\ \eta_{x_i} (u_j \tau_{ij} - Q_i) \end{bmatrix}, \quad H_v = \frac{1}{J} \begin{bmatrix} 0 \\ \zeta_{x_i} \tau_{i1} \\ \zeta_{x_i} \tau_{i2} \\ \zeta_{x_i} \tau_{i3} \\ \zeta_{x_i} (u_j \tau_{ij} - Q_i) \end{bmatrix} \quad (4)$$

where

$$U = \xi_t + \xi_{x_i} u_i, \quad V = \eta_t + \eta_{x_i} u_i, \quad W = \zeta_t + \zeta_{x_i} u_i \quad (5)$$

$$E = \frac{T}{\gamma(\gamma-1)M_\infty^2} + \frac{1}{2} (u^2 + v^2 + w^2). \quad (6)$$

In the preceding expressions, u, v, w are the Cartesian velocity components, ρ the density, p the pressure, and T the temperature. All length scales have been nondimensionalized by the turbine blade axial chord c , and dependent variables have been normalized by their reference values except for p which has been nondimensionalized by $\rho_\infty u_\infty^2$. Components of the stress tensor and heat flux vector are expressed as

$$Q_i = - \left[\frac{1}{(\gamma-1)M_\infty^2} \right] \left(\frac{\mu}{Pr} \right) \frac{\partial \xi_j}{\partial x_i} \frac{\partial T}{\partial \xi_j} \quad (7)$$

$$\tau_{ij} = \mu \left(\frac{\partial \xi_k}{\partial x_j} \frac{\partial u_i}{\partial \xi_k} + \frac{\partial \xi_k}{\partial x_i} \frac{\partial u_j}{\partial \xi_k} - \frac{2}{3} \delta_{ij} \frac{\partial \xi_l}{\partial x_k} \frac{\partial u_k}{\partial \xi_l} \right). \quad (8)$$

The Sutherland law for the molecular viscosity coefficient μ and the perfect gas relationship

$$p = \frac{\rho T}{\gamma M_\infty^2} \quad (9)$$

were also employed, and Stokes' hypothesis for the bulk viscosity coefficient has been invoked.

3 The Numerical Method

Time-accurate solutions to Eq. (1) are obtained numerically by the implicit approximately-factored finite-difference algorithm of Beam and Warming[30] employing Newton-like subiterations,[31] which has evolved as an efficient tool for generating solutions to a wide variety of complex fluid flow problems, and may be written as follows

$$\begin{aligned} & \left[\frac{1}{\mathcal{J}} + \left(\frac{2\Delta t}{3} \right) \delta_{\xi 2} \left(\frac{\partial F^p}{\partial Q} - \frac{1}{Re_\infty} \frac{\partial F_v^p}{\partial Q} \right) \right] \mathcal{J} \times \left[\frac{1}{\mathcal{J}} + \left(\frac{2\Delta t}{3} \right) \delta_{\eta 2} \left(\frac{\partial G^p}{\partial Q} - \frac{1}{Re_\infty} \frac{\partial G_v^p}{\partial Q} \right) \right] \mathcal{J} \times \\ & \left[\frac{1}{\mathcal{J}} + \left(\frac{2\Delta t}{3} \right) \delta_{\zeta 2} \left(\frac{\partial H^p}{\partial Q} - \frac{1}{Re_\infty} \frac{\partial H_v^p}{\partial Q} \right) \right] \Delta Q = - \left(\frac{2\Delta t}{3} \right) \left[\left(\frac{1}{2\Delta t} \right) \left(\frac{3Q^p - 4Q^n + Q^{n-1}}{\mathcal{J}} \right) \right. \\ & \left. + \delta_{\xi 4} \left(F^p - \frac{1}{Re_\infty} F_v^p \right) + \delta_{\eta 4} \left(G^p - \frac{1}{Re_\infty} G_v^p \right) + \delta_{\zeta 4} \left(H^p - \frac{1}{Re_\infty} H_v^p \right) \right]. \end{aligned} \quad (10)$$

In this expression, which is employed to advance the solution in time, Q^{p+1} is the $p + 1$ approximation to Q at the $n + 1$ time level Q^{n+1} , and $\Delta Q = Q^{p+1} - Q^p$. For $p = 1$, $Q^p = Q^n$. Second-order-accurate backward-implicit time differencing was used to obtain temporal derivatives.

The implicit segment of the algorithm incorporates second-order-accurate centered differencing for all spatial derivatives, and utilizes nonlinear artificial dissipation[32] to augment stability. Efficiency is enhanced by solving this implicit portion of the factorized equations in diagonalized form.[33] Temporal accuracy, which can be degraded by use of the diagonal form, is maintained by utilizing subiterations within a time step. This technique has been commonly invoked in order to reduce errors due to factorization, linearization, diagonalization, and explicit application of boundary conditions. It is useful for achieving temporal accuracy on overset zonal mesh systems, and for a domain decomposition implementation on parallel computing platforms. Any deterioration of the solution caused by use of artificial dissipation and by lower-order spatial resolution of implicit operators is also reduced by the procedure. Three subiterations per time step have been applied to preserve second-order temporal accuracy.

The compact difference scheme employed on the right-hand side of Eq. 10 is based upon the pentadiagonal system of Lele,[34] and is capable of attaining spectral-like resolution. This is achieved through the use of a centered implicit difference operator with a compact stencil, thereby reducing the associated discretization error. For the present computations, a fourth-order tridiagonal subset of Lele's system is utilized, which is illustrated here in one spatial dimension as

$$\alpha \left(\frac{\partial F}{\partial \xi} \right)_{i-1} + \left(\frac{\partial F}{\partial \xi} \right)_i + \alpha \left(\frac{\partial F}{\partial \xi} \right)_{i+1} = a \left(\frac{F_{i+1} - F_{i-1}}{2} \right) \quad (11)$$

with $\alpha = 1/4$ and $a = 3/2$. The scheme has been adapted by Visbal and Gaitonde[35] as an implicit iterative time-marching technique, applicable for unsteady vortical flows. It is used in conjunction with a sixth-order low-pass Pade-type non-dispersive spatial filter developed by Gaitonde et al.,[36] which has been shown to be superior to the use of explicitly added artificial dissipation for maintaining both stability and accuracy on stretched curvilinear meshes.[35] The filter is applied to the solution vector sequentially in each of the three computational directions following each subiteration, and is implemented in one dimension as

$$\alpha_f \hat{Q}_{i-1} + \hat{Q}_i + \alpha_f \hat{Q}_{i+1} = \sum_{n=0}^3 \frac{a_n}{2} (Q_{i+n} + Q_{i-n}) \quad (12)$$

where \hat{Q} designates the filtered value of Q . Equation 12 represents a one-parameter family of sixth-order filters, where numerical values for α_f and the a_n 's may be found in Ref. Gaitonde:AFRL3060

The aforementioned features of the numerical algorithm are embodied in a parallel version of the time-accurate three-dimensional computer code FDL3DI,[37] which has proven to be reliable for steady and unsteady fluid flow problems, including the simulation of flows over delta wings with leading-edge vortices,[38, 39, 40] vortex breakdown,[39, 40] direct numerical simulation of transitional wall jets[41] and synthetic jet actuators,[42] and DNS and LES of subsonic[24, 43] and supersonic flowfields.[44, 45, 46]

4 Details of the Computations

The experiment Sondergaard et al.[13] consisted of a linear cascade of turbine blades having a span of 0.88 m and an axial chord of 0.089 m. The axial chord to spacing ratio (solidity) was 0.75, the inlet flow angle $\alpha_i = 35.0$ deg, and the design exit flow angle $\alpha_o = 60.0$ deg. Shown in Fig. 1 is a schematic representation of the turbine blade shape, given by the Pratt & Whitney “PakB” research design, which is a Mach number scaled version of geometries typically used in highly-loaded low-pressure turbines.[10, 11, 12, 15, 13] These experiments investigated the use of vortex generator jets to control the flow by mitigating the effects of separation on the blade suction surface. The jets were created by blowing air through holes which had been drilled in the blade surface at a pitch angle of 30 deg and a skew angle of 90 deg. Here, the pitch is defined as the angle the jet makes with the local surface, and the skew is the angle of the projection of the jet on the surface, relative to the “local freestream” direction.[12] The size of the drill used to develop the holes is commonly referred to as the jet diameter d , which was 0.001 m. Because of the orientation however, the jet exit geometric shape is elliptic as seen in Fig. 2, and the jet exit velocity vector has components only in the blade-normal (n) and spanwise (z) directions.

4.1 Computational Meshes

To conserve computational resources, only a single turbine blade passage is considered, and periodic conditions are enforced in the vertical direction (y) to represent a single turbine stage flowfield. This situation is somewhat different than the experimental arrangement, which consisted of a small finite number of blades in a linear cascade. The computational domain surrounding the blade was described by a body-fitted mesh system, whose origin was located at the inboard leading edge of the blade (see Fig. 1). The mesh employs an O-grid topology, and was elliptically generated using automated software.[47] Figure 3 indicates the baseline grid about the turbine blade, which was comprised of 348 points in the circumferential direction (I), 189 points in the blade-normal direction (J), and 101 points in the spanwise direction (K). Minimum spacing in the J -direction occurs at the blade surface. Mesh points for $1 \leq I \leq 5$ and $I_{\max}-4 \leq I \leq I_{\max}$ are coincident in an overlap region at the blade leading edge so that periodic conditions in the circumferential direction may be enforced in order to complete the O-grid construct. To accommodate periodic conditions in the vertical direction, the streamwise (x) point locations and vertical spacing along $I_{1u} - I_{2u}$ is identical to that along $I_{1l} - I_{2l}$ for $J_{\max}-4 \leq J \leq J_{\max}$.

To properly capture the correct fluid physics for the flow control cases, the baseline grid was modified in order to enhance resolution in the jet and jet wake regions. This was done by removing points in the near wall grid, indicated by the blanked area of Fig. 3, and replacing them with an embedded refined mesh as seen in Fig. 4. This technique is identical to that which was successfully employed by Rizzetta and Visbal[27] in a similar computation. The size of the refined mesh region was $(313 \times 185 \times 101)$ grid points in (I, J, K) respectively. A series of overset grids were used to describe the elliptic jet geometry, and zones upstream, downstream, inboard, and outboard of the jet. These grids connect to each other and with the refined-mesh region as shown in Fig. 5. Also seen in the figure is the jet nozzle interior to the blade, which was accounted for in the simulations, and extended a distance of four jet diameters below the surface.

In order to facilitate application of inflow and outflow conditions to the turbine blade domain, overset grids were utilized upstream and downstream of the blade region. These are found in Fig. 6, and consisted of $(46 \times 61 \times 101)$ and $(31 \times 75 \times 101)$ mesh points in the streamwise, vertical, and spanwise directions for the upstream and downstream domains respectively. Half the grid points in the vertical direction are seen in the figure. Although the experiment of Sondergaard et al. [15] consisted of a row of jets uniformly distributed along the span of a blade, only a single jet was considered in the simulations. The z -extent of the domain was taken as the inter-jet spacing $s = 0.112$, which is equal to 10 jet diameters (as in the experiment) and periodic conditions were invoked at the spanwise boundaries. A non-uniform spanwise mesh distribution was utilized, with grid point clustering near the jet exit. At all overset domain boundaries, a minimum 5-point overlap was constructed. The total number of grid points in all domains was approximately 13.5×10^6 . Computational mesh spacings given in wall units for both simulations are presented in Table 1. Results of the grid refinement study performed for the baseline uncontrolled case of Ref. Rizzetta:2004-2204, indicates that adequate resolution should be achieved for the present computations.

Table 1: Computational mesh spacings in wall units.

Case	Δt^+	Δl_{\min}^+	Δl_{\max}^+	Δn_{\min}^+	Δz_{\min}^+	Δz_{\max}^+
steady	0.02	1.63	50.07	0.44	3.09	10.98
pulsed	0.02	1.74	53.39	0.46	3.23	11.47

4.2 Temporal Considerations

Calculations for the steady jet case were obtained using a time step of $\Delta t = 1.50 \times 10^{-4}$, where t is nondimensionalized by reference quantities. Based upon inflow conditions, this corresponds to a time increment of approximately 1.18×10^{-4} (see Table 1 for the time step in wall units). For the pulsed case, these parameters were $\Delta t = 1.47 \times 10^{-4}$ and $\Delta t_i = 1.20 \times 10^{-4}$ respectively. A slightly smaller time step was employed with unsteady injection so that the pulsing cycle could be described by an integer number of increments (1300 time steps/cycle). Flowfields for each case were initialized from the previously obtained baseline (uncontrolled) solution, and processed for 20,000 time steps in order to remove transients. Final results were then evolved for a subsequent 124,000 steps, during which statistical information was collected. Statistics were monitored to assure that a converged sample was achieved. This duration represents over 14.5 characteristic time units, based upon the inflow velocity, for both simulations.

Experimental investigations[10, 11, 12, 15, 13] have used several parameters to describe characteristics of vortex generating jets. The jet blowing ratio B is defined as

$$B = \frac{q_j}{\bar{q}_l} \quad (13)$$

where q_j is the jet exit velocity magnitude, and \bar{q}_l is the “local freestream velocity” (see Ref. Bons:JTM2001 for the definition of \bar{q}_l). In the present computations, the maximum value of the jet blowing ratio B_{\max} was specified as 4.5. This is identical to the experiment of Sondergaard et al.[15] for the steady case. As a point of reference, typical film cooling holes for turbine applications are designed to operate at an approximate value of $B_{\max} = 2.0$. [12] For the present configuration considered here, experimental data is available only for steady blowing flow control. In previous investigations with a smaller inter-blade spacing however, measurements were also taken using pulsed mass injection. The unsteady jet exit velocity sequence in those experiments consisted of a period of essentially constant blowing, followed by an interval of no blowing. The duty cycle represents that portion of the total duration over which the jet is active, and was 50% for the present case. A nondimensional frequency \mathcal{F} as formulated in Refs. Bons:99-0367, Bons:JTM2001, Bons:JTM2002, Sondergaard:JPP2002 was used to quantify the forcing period where

$$\mathcal{F} = 0.41cf/u_{\infty}\bar{q}_l. \quad (14)$$

The value of $\mathcal{F} = 3.1$ was used in the present computations, which was the same as that of some experiments[10, 11, 12]. The jet blowing coefficient, defined as

$$c_{\mu} = \mathcal{D} [(\pi/4)d^2 B_{\max}^2] \quad (15)$$

is used to quantify the momentum flux transferred to the turbine blade passage by active control. For the steady blowing case $c_{\mu} = 2.0 \times 10^{-3}$, and is one half this value for pulsed injection owing to the 50% duty cycle.

A representative experimental[12] time history of one blowing cycle obtained by hot wire measurement is shown in Fig. 7. For the pulsed-injection computation, a series of cubic and linear functions were used to approximate the experimental result, as seen in the figure where the 50% duty cycle is apparent. As noted earlier, a single cycle was described by 1300 time steps, and the total computation consisted of 96 cycles.

4.3 Boundary Conditions

Inflow and outflow conditions for the complete turbine blade domain were obtained in a manner consistent with subsonic internal flows, which have commonly been employed in RANS applications.[48] Along the

upstream boundary, the total pressure, total temperature, and inlet flow angle were specified, and the velocity magnitude was obtained from the interior solution. Downstream, the exit static pressure (p_∞) was fixed, and other flow variables were extrapolated from within the domain. Because the inflow velocity develops as part of the solution, the Reynolds number based upon the inflow conditions was not known a priori. A reference Mach number (M_∞) of 0.1 was selected for all computations. For the baseline solution, the reference Reynolds number (Re_∞) was adjusted to match the desired inflow condition, Re . This same Reynolds number was then employed in the current simulations. When flow control was applied however, the inflow velocity magnitude increased due to a reduction of blockage in the blade passage. Although this situation was anticipated, the reference Reynolds number was not altered. Thus, the inflow Reynolds numbers are somewhat higher than the nominal value of 25,000. For the time-mean flowfields, $Re = 29,100$ for steady blowing and $Re = 29,960$ with pulsed mass injection. This approach for the inflow and outflow boundaries was previously employed by Rizzetta and Visbal[24, 27] in similar computations.

Periodic conditions were applied along the upper and lower portions of the turbine blade as indicated previously in Fig. 3. Periodic conditions were also applied along upper and lower horizontal boundaries of the upstream and downstream domains seen in Fig. 6. The downstream domain was intentionally severely stretched in the streamwise direction to prevent spurious reflections from the outflow boundary. This technique transfers information to high spatial wave numbers, and then dissipates it by the low-pass filter.[49] Flow variables in all regions of overlapped meshes were obtained from explicit sixth-order accurate Lagrangian interpolation formulae. This includes the upstream and downstream domains, the turbine blade grid, the refined-mesh region, all zones surrounding the jet, and the interior jet nozzle. The interpolation approach for high-order numerical solutions has been successfully applied by Sherer[50] for the simulation of fluid dynamic and acoustic problems. As stated previously, periodic conditions were invoked in the spanwise direction.

On solid surfaces, including the blade boundary and walls of the jet nozzle, the no slip condition was enforced along with an isothermal wall, and a fourth-order accurate representation of zero normal pressure gradient. At the inflow to the jet nozzle, a velocity profile was specified, the jet was assumed to be isothermal, and the pressure was obtained from the inviscid normal momentum equation. For both the steady and pulsed cases, the velocity profile was taken to be parabolic. In the steady case, the maximum jet blowing ratio was fixed at $B_{\max} = 4.5$, corresponding to the experiment, while for pulsed injection this ratio varied in time according to the form shown in Fig. 7. It is noted for both cases that the maximum jet velocity is over seven times greater than the magnitude of the blade inflow velocity. The Reynolds number of the jet based upon the maximum blowing ratio and the diameter d was 2370.

4.4 Domain Decomposition

For parallel processing, the previously described computational domains were decomposed into a series of subzones, which were then distributed on individual processors of a massively parallel computing platform (IBM SP4, SGI 3900). Decompositions were constructed to provide an approximately equal number of grid points in every subzone, thereby balancing the computational work load among the processors. Faces at the boundaries of each subzone block were overset into adjacent domains, such that an overlap of five planes was established. Although this incurred an overhead due to redundant computation, it maintained the formal high-order accuracy of both the numerical differencing and filtering schemes. Because a vast majority of the overlapping mesh points of the respective decompositions were coincident, no further interpolation was required. Automated software[51] was used to identify donor and recipient grid points in the overlapping domains. Inter-node communication among the processors was established through standard message-passing interface (MPI) library routines,[52] which were used to transfer information between the various subzones of the flowfield at domain boundaries. A total of 202 processors were employed for all of the computations reported here.

5 Results

5.1 The Time-Mean Flowfields

Time-mean surface pressure coefficient distributions for the flow control and baseline[27] computations are found in Fig. 8. For the flow control cases, these distributions were obtained at the spanwise location of the periodic boundary between two jets. As indicated in the figure, the jet was positioned at $x = 0.37$, which coincides with the separation point of the baseline solution. The large plateau region in the baseline distribution is characteristic of massively separated flow. Because of reduced blockage and increased inflow velocity, the effect of flow control is to decrease the pressure on the upstream portion of the suction surface, while increasing it downstream, relative to the baseline case. Separation occurs at $x = 0.56$ for the steady blowing result, and at $x = 0.58$ for pulsed injection. Only minor differences, most noticeable near the jet, are observed between the two flow control solutions. Also shown in the figure, is a coarse-mesh distribution for the baseline case, which indicates little sensitivity to grid resolution, except near the trailing-edge region. More extensive results of the grid resolution study for the baseline case are found in Ref. Rizzetta:2004-2204.

Profiles of the time-mean velocity magnitude are presented in Figs. 9 and 10. These profiles were extracted along lines (n) normal to the blade surface at each x -station, on the periodic spanwise boundary between jets. The data of Sondergaard et al. [15] for steady blowing also appears in the figures. However, only a qualitative comparison between the experimental and numerical results may be expected due to appreciable differences in the respective flow situations. Among these are the fact that the experiments were conducted in a linear cascade, which had a limited number of blades because of the large inter-blade spacing. Tail boards were attached at the trailing edge of the first and last blades in the cascade, and extended downstream a considerable distance into the wake, thus creating covered turning for a substantial portion of the flowfield. Vortex generating jets were fabricated only on the central blade of the cascade. This arrangement is quite unlike the simulations, where periodic conditions about the blade are enforced. The computations were carried out at a nominal Reynolds number of 25,000 which is representative of the practical situation for UAVs, and may be compared with the previously obtained baseline case. Experimental data was collected for $Re = 50,000$.

Profiles in Figs. 9 and 10 have been normalized by the inflow velocity magnitude. The major effect of flow control is to increase fullness of the profiles through momentum transfer from the jet and mixing with the boundary layer. Only minor variations are observed between the steady and pulsed injection cases. As expected, profiles from the simulations are thicker than those of the experiment due to aforementioned differences in the Reynolds numbers and configurations. Increased fullness of the control profiles from the baseline solution is evident in the figures, even at locations where separation is present ($x > 0.58$).

Spanwise turbulent kinetic energy wave-number spectra are provided in Fig. 11. These spectra were generated along lines in the z -direction at a distance of $n = 0.03$ from the blade surface. This location ($n = 0.03$) is approximately equal to one half of the boundary-layer thickness of the time-mean velocity profile upstream of separation. At the two most upstream stations ($x = 0.50, 0.70$), E_{k_z} is higher for the flow control cases than that of the baseline due to energy being added to the flow. In the downstream region ($x = 0.90$), flow control has mitigated separation and the associated breakdown into a more chaotic situation, so that the turbulent kinetic energy of the baseline case is higher. Because of the low Reynolds number, only a small portion of the spectrum at low wave number lies in the inertial range.

Time-mean contours of the streamwise component of velocity u , are seen in Fig. 12. The contours for the flow control results were taken at the plane of the periodic boundary between jets, while those of the baseline case have been spanwise averaged. An increased region of attached flow due to flow control is apparent, resulting in a decrease of the wake thickness. The effect of the decrease is quantified by the integrated wake total pressure loss coefficient C_w , defined as[15]

$$C_w = S \int \left(\frac{P_{ti} - \bar{P}_{to}}{P_{ti} - \bar{p}_i} \right) dy \quad (16)$$

where the integration takes place across the wake profile between the periodic boundaries in the vertical direction. It was determined that $C_w = 1.10$ [27] for the baseline solution, $C_w = 0.52$ for steady blowing, and $C_w = 0.48$ for pulsed injection. Thus even with a 50% duty cycle, pulsed injection was found to be as effective as steady blowing for the reduction of wake losses. This result is consistent with previous

experimental studies.[11, 12]

Corresponding time-mean contours of the spanwise component of vorticity are displayed in Figure 13. Maintaining attached flow and decreasing the extent of the wake are again exhibited by the flow control results. Fig. 14 represents these same contours evaluated on the blade surface and viewed from above. Apart from the area immediately surrounding the jet, the flow control cases are remarkably similar.

5.2 Unsteady Features of the Flowfields

Profiles of the root-mean-square fluctuating velocity magnitude at several streamwise locations are found in Fig. 15. At the upstream stations ($x = 0.50, 0.70$), the flow control cases differ somewhat from each other, but both produce peak values less than that of the baseline result. Fluctuations in the control cases are related to unsteadiness of the jet, while those of the baseline flow evolve from the shear layer. As a result, the location of the maximum fluctuation occurs further from the blade surface in the baseline solution. At the downstream location ($x = 0.90$), a more massive separated region in the baseline flow gives rise to a uniformly high fluctuating velocity in the normal direction, which is more localized in the flow control cases.

Turbulent kinetic energy frequency spectra are shown in Fig. 16. The data used to generate these spectra was collected at $n = 0.03$, similar to that of Fig. 11. Like the spanwise wave number spectra of Fig. 11, the frequency spectra for the flow control cases is substantially higher than that of the baseline result at the upstream stations ($x = 0.50, 0.70$) because of energy addition. At $x = 0.50$, the discrete peaks in E_ω for the pulsed injection case correspond to harmonics of the forcing frequency. The occurrence of this behavior was described in detail in Ref. Rizzetta:2004-2204. As noted previously, turbulent energy of the baseline case exceeds that of the flow control results near the blade trailing edge ($x = 0.90$).

Instantaneous contours of the streamwise velocity component u are presented Fig. 17. The baseline result was extracted at the midspan location, while those of the flow control cases were situated between control jets. Similar to the time-mean contours of Fig. 12, it is noted that flow control maintains attached flow and decreases the vertical extent of the wake relative to the baseline case. Unsteady structures are visible in separated flow regions. These structures are more easily discerned in instantaneous spanwise vorticity contours appearing in Fig. 18. It is seen in the flow control cases that vorticity is being generated in the boundary layer in close proximity to the blade surface. When the boundary layers separate in these situations, it is much less dramatic than in the uncontrolled case. For the baseline solution, the extensive unsteady separated flow region has a richer content of small scale structures due to breakdown and a transition to a more complex situation. A three-dimensional representation of the flow is depicted by iso-surfaces of vorticity magnitude in the trailing-edge region seen in Fig. 19. The value of iso-surfaces correspond approximately to that at the edge of the shear layer upstream of separation. Both the vertical and spanwise extent of the turbulent structures are visible for each case.

Instantaneous spanwise vorticity contours on the blade surface viewed from above are displayed in Fig. 20. Although differences in the control case exist in the near-jet region, the downstream flowfields are quite similar. Iso-surfaces of vorticity magnitude in the near-jet region, as viewed downstream of the jet, are provided in Fig. 21. Unsteadiness can be observed in the jet surface, just downstream of the nozzle exit, for the steady blowing case. It is noted that the wake of the jet extends across the spanwise domain. The jet surface for the pulsed case is less coherent.

Instantaneous planar contours of the streamwise component of vorticity are found in Figs. 22-24. Locations of these contours lie at distances of 1, 5, and 10 jet diameters downstream from the center of the jet. The height of the attached boundary layer (δ) upstream of the jet is indicated in the figures. For the steady injection case of Fig. 22, the jet penetrates to a height greater than the boundary-layer thickness, and mixing persists downstream beyond $x - x_j = 10d$. In Fig. 23, contours are shown for the pulsed case, at a time corresponding to the midpoint of the pulsing cycle ($t/t_p = 0.5$). At this instance, the jet exit velocity is at its maximum and has been active for one half the cycle (see Fig. 7). Here, the contours look similar to those of the steady injection case, except at the most downstream station. Contours for the pulsed case at the end of the injection cycle appear in Fig. 24. For this situation ($t/t_p = 1.0$), no injection has occurred for one half of the cycle, and effects of the jet are only visible at the most downstream station.

It is perhaps surprising that there are so few differences between the steady blowing and pulsed injection cases. The reason for this is that even in the steady case, the flow immediately downstream of the jet is inherently unsteady. Because of the orientation of the jet transverse to the streamwise flow (blade-normal

and spanwise), it is fundamentally unstable and rapidly evolves to a non-coherent form. This process serves to generate mixing, much like the pulsed injection case. The pulsed case however, provides a much more efficient means of distributing momentum to the flow, since it produces identical benefits with one half the mass flow rate.

6 Summary and Conclusion

Direct numerical simulation was used to describe the transitional subsonic flow through a highly-loaded low-pressure turbine at a nominal Reynolds number of 25,000, with both steady blowing and pulsed mass injection flow control. Computations were carried out using a high-order numerical method, and an overset grid methodology for describing the computational flowfield. A high-order interpolation procedure maintained accuracy at boundaries of discrete mesh systems that were used to define the jet region, including its interior nozzle.

For both the steady and pulsed cases, the fundamental effect of flow control was to energize the blade boundary layer due to the transfer of fluid momentum and mixing. This helped maintain attached flow along the blade surface for a distance of 19-21% greater than that of the baseline case. As a result, wake total pressure losses were decreased by 53-56%.

Comparisons were made for both the time-mean and fluctuating components of the respective flowfields. Velocity magnitude profiles qualitatively agreed with experimental measurements that were taken for a somewhat different configuration at a higher Reynolds number. Few differences were observed in characteristics of the flow control solutions. Although the steady blowing case employed no explicit unsteady forcing, due to fluid instability of the jet, the flowfield was inherently unsteady and resulted in features which were quite similar to the pulsed case. Both situations achieved the desired result of decreased wake losses, but the pulsed case required less mass flow to attain the same level of improvement in efficiency.

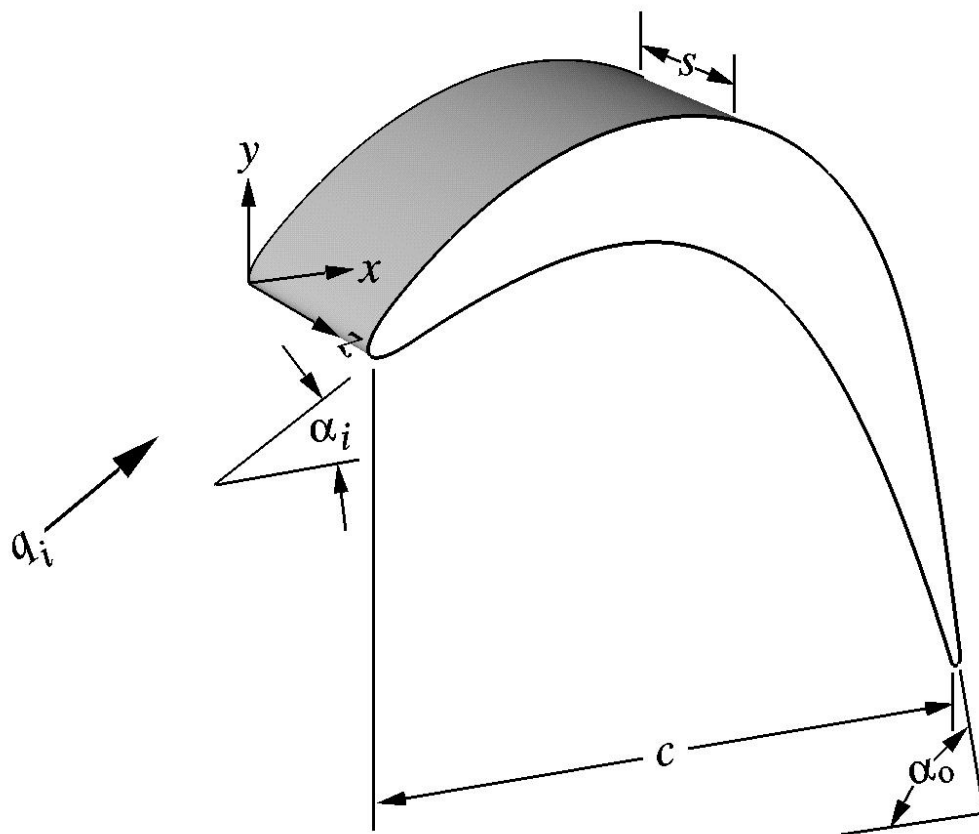


Figure 1: Schematic representation of the turbine blade configuration.

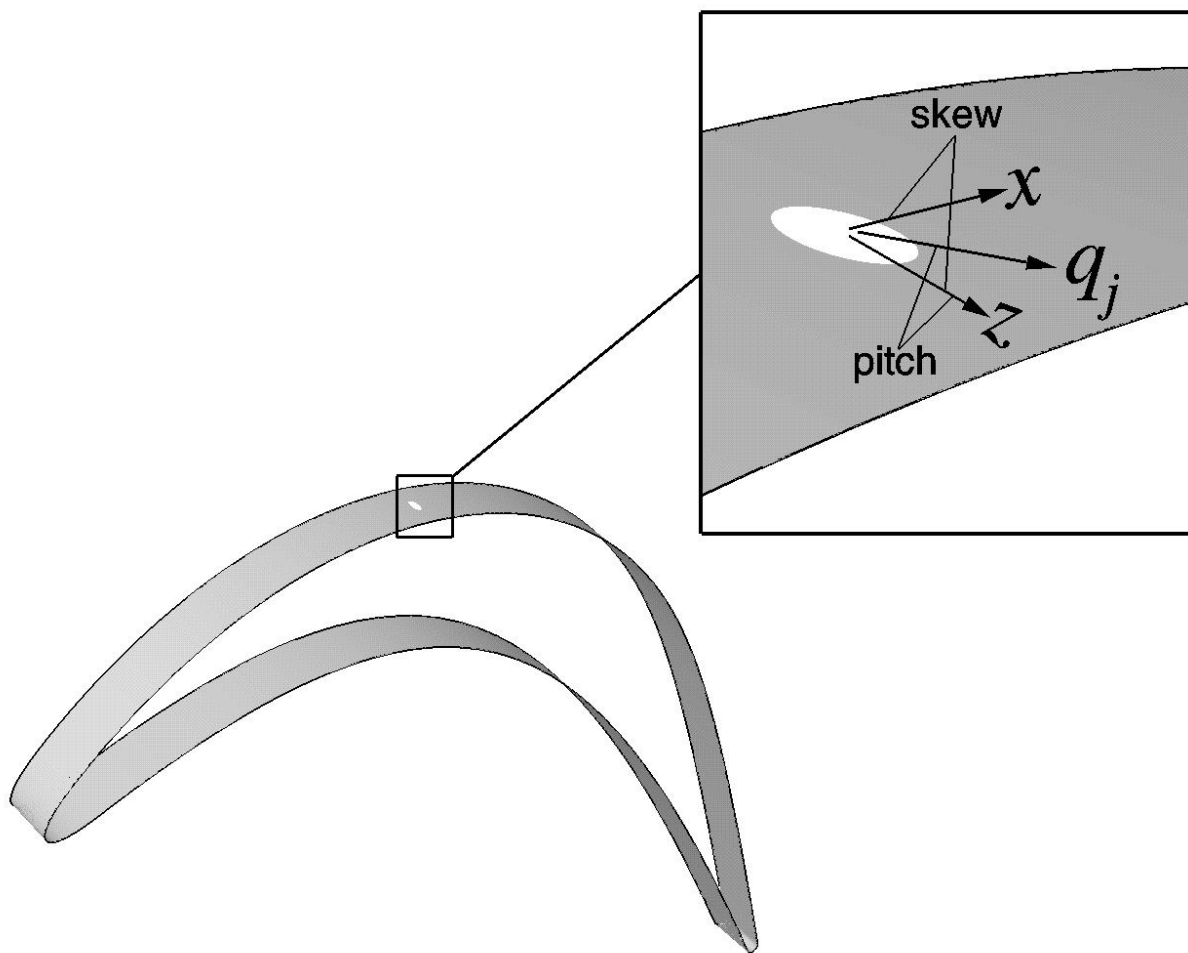


Figure 2: Vortex generator jet geometry.

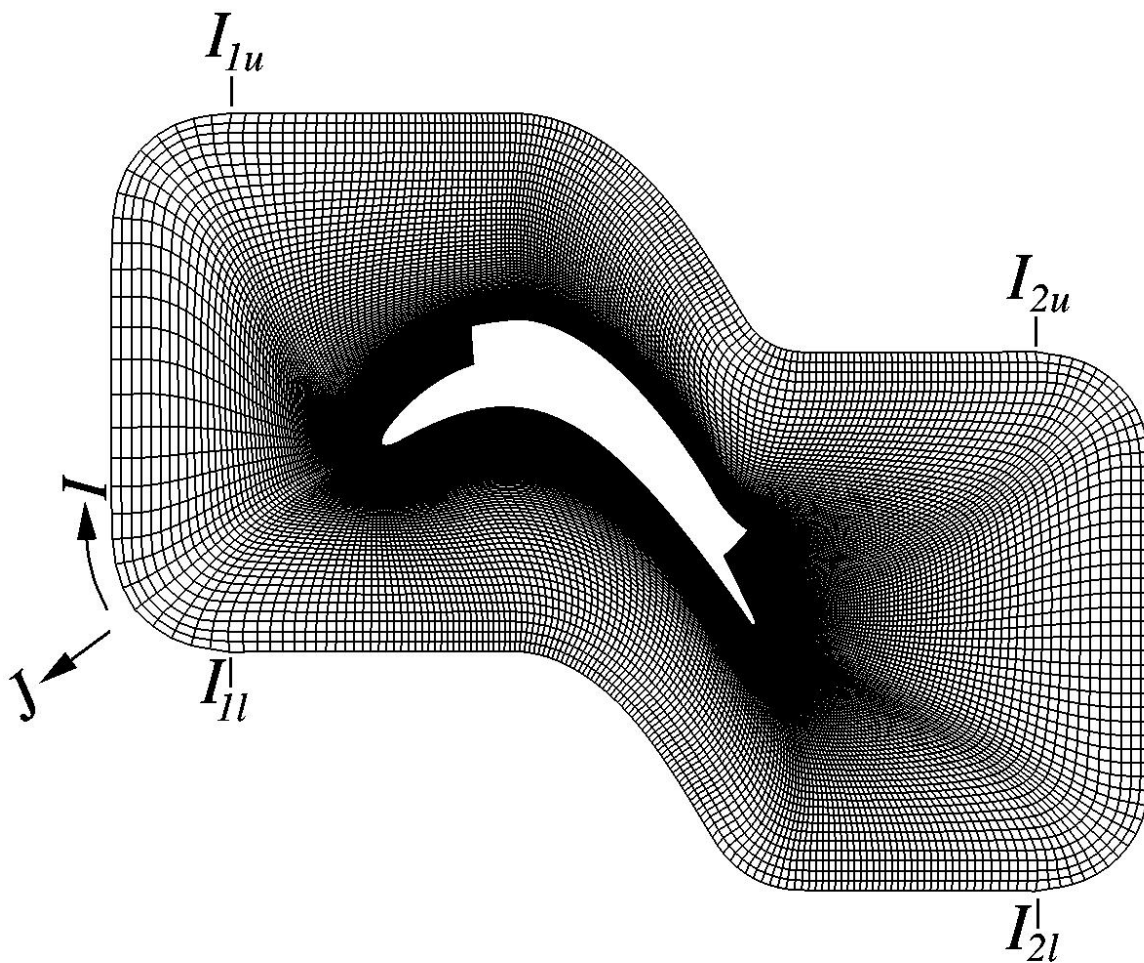


Figure 3: Turbine blade computational mesh.

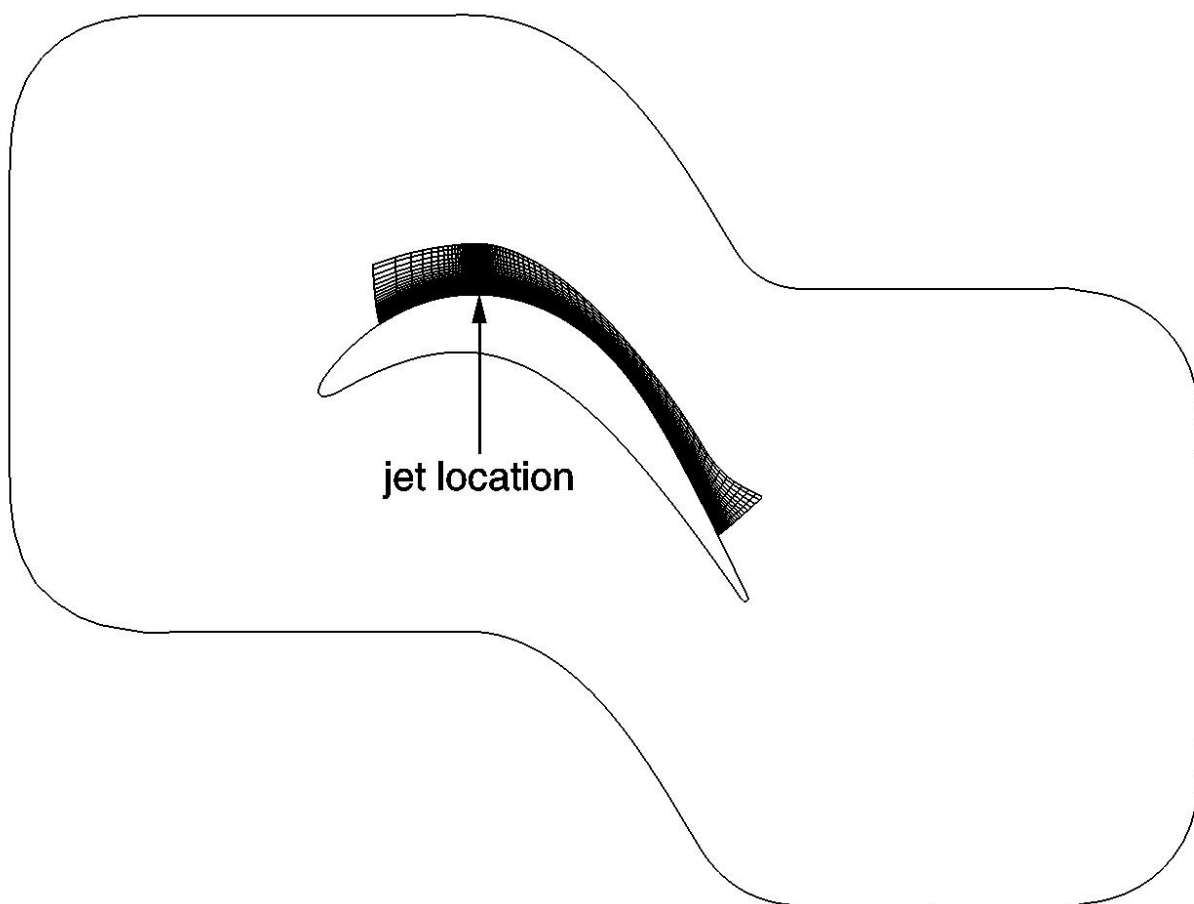


Figure 4: Refined-mesh region.

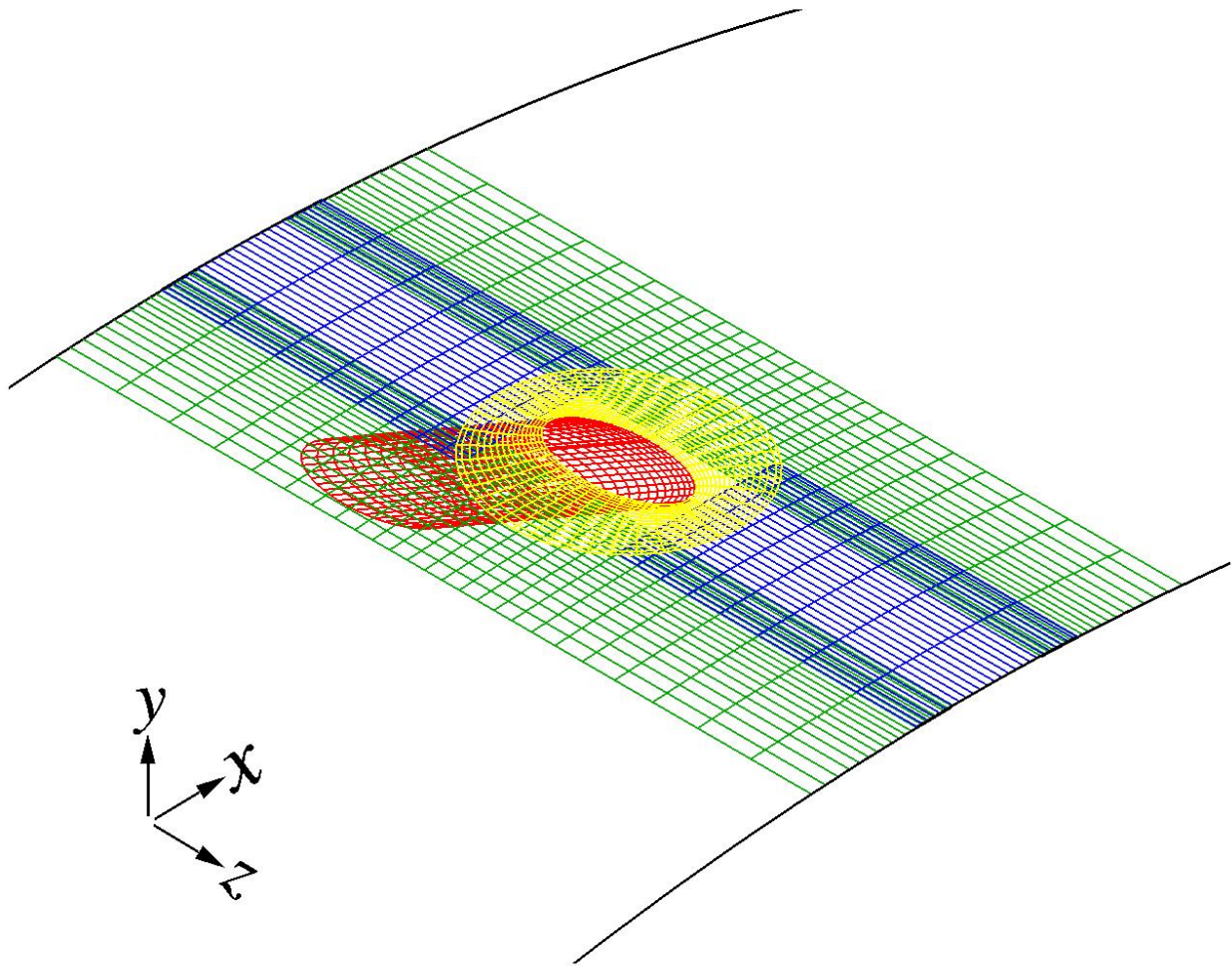


Figure 5: Vortex-generator jet region.

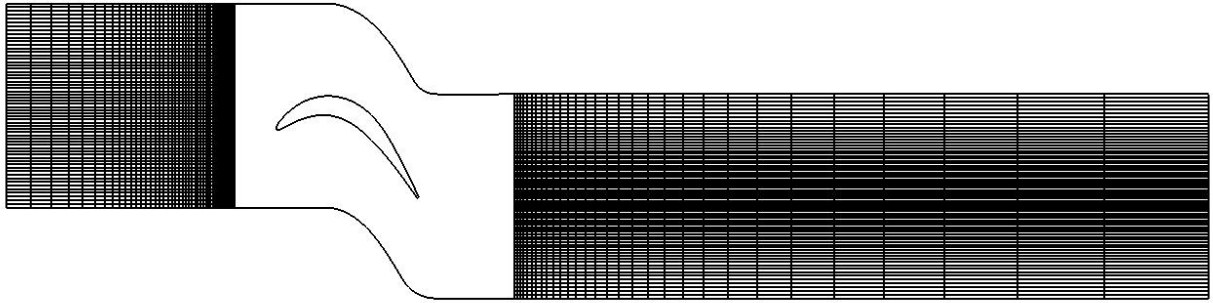


Figure 6: Upstream and downstream computational meshes.

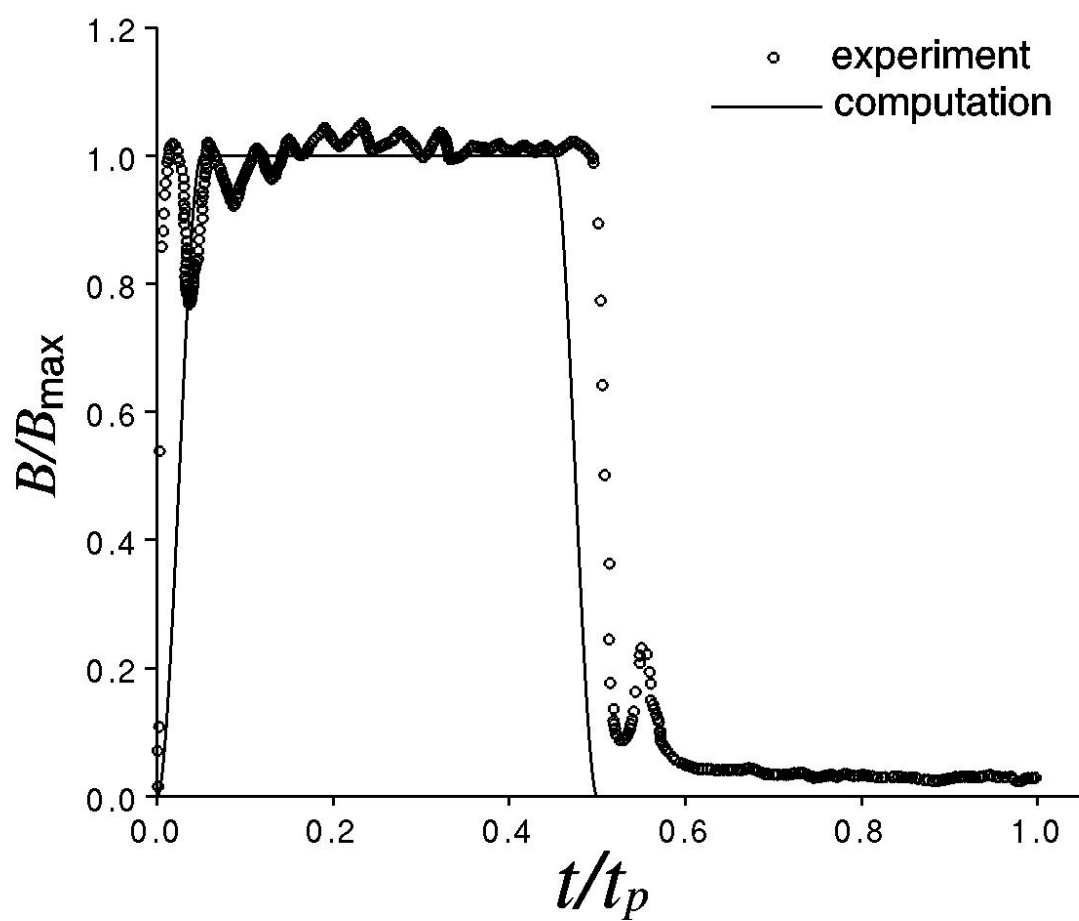


Figure 7: Jet blowing ratio time history.

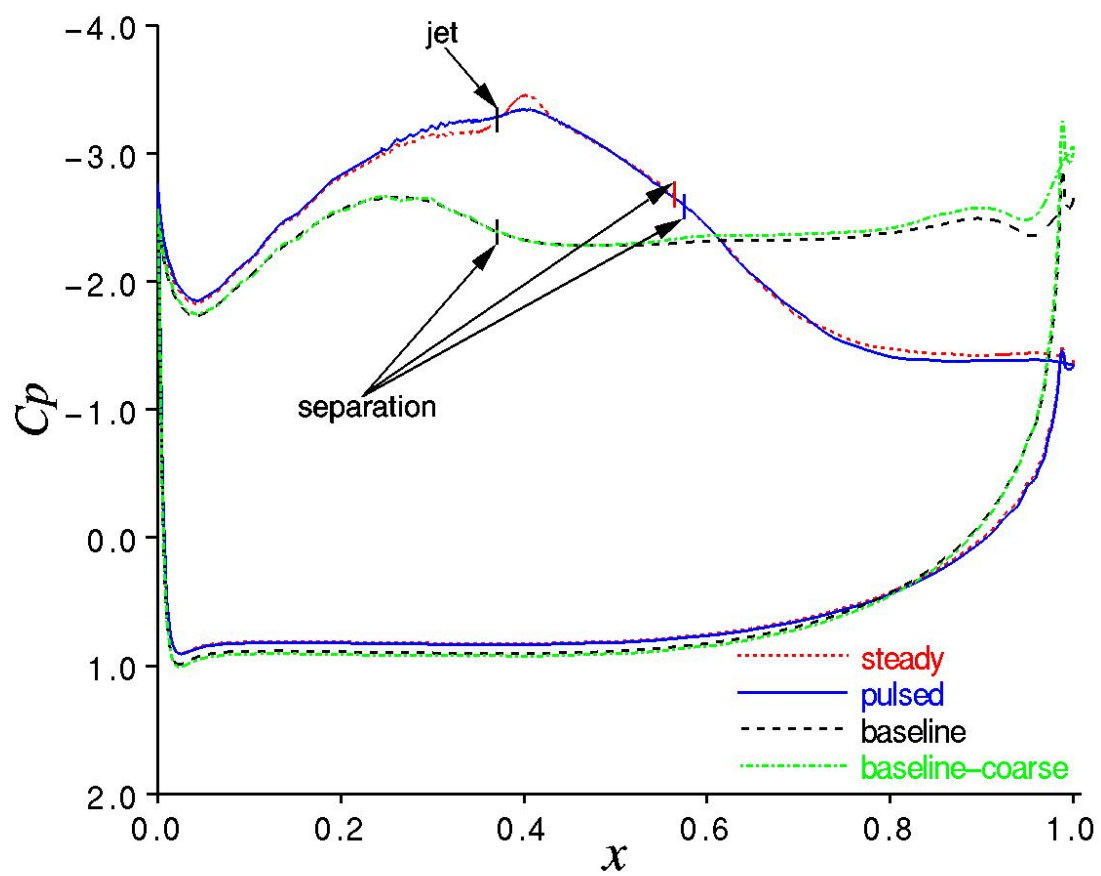


Figure 8: Time-mean surface pressure coefficient distributions.

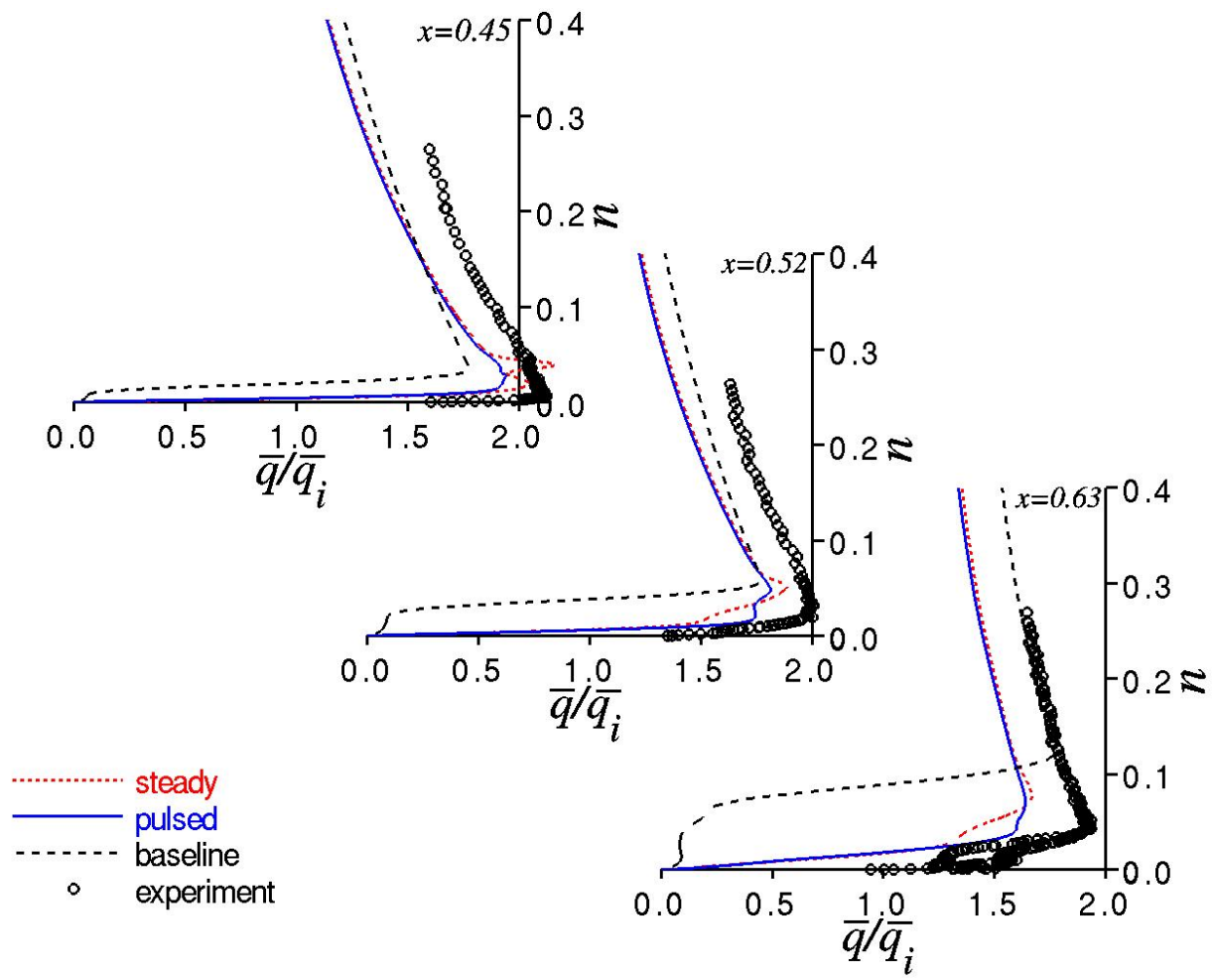


Figure 9: Time-mean velocity magnitude profiles at upstream stations.

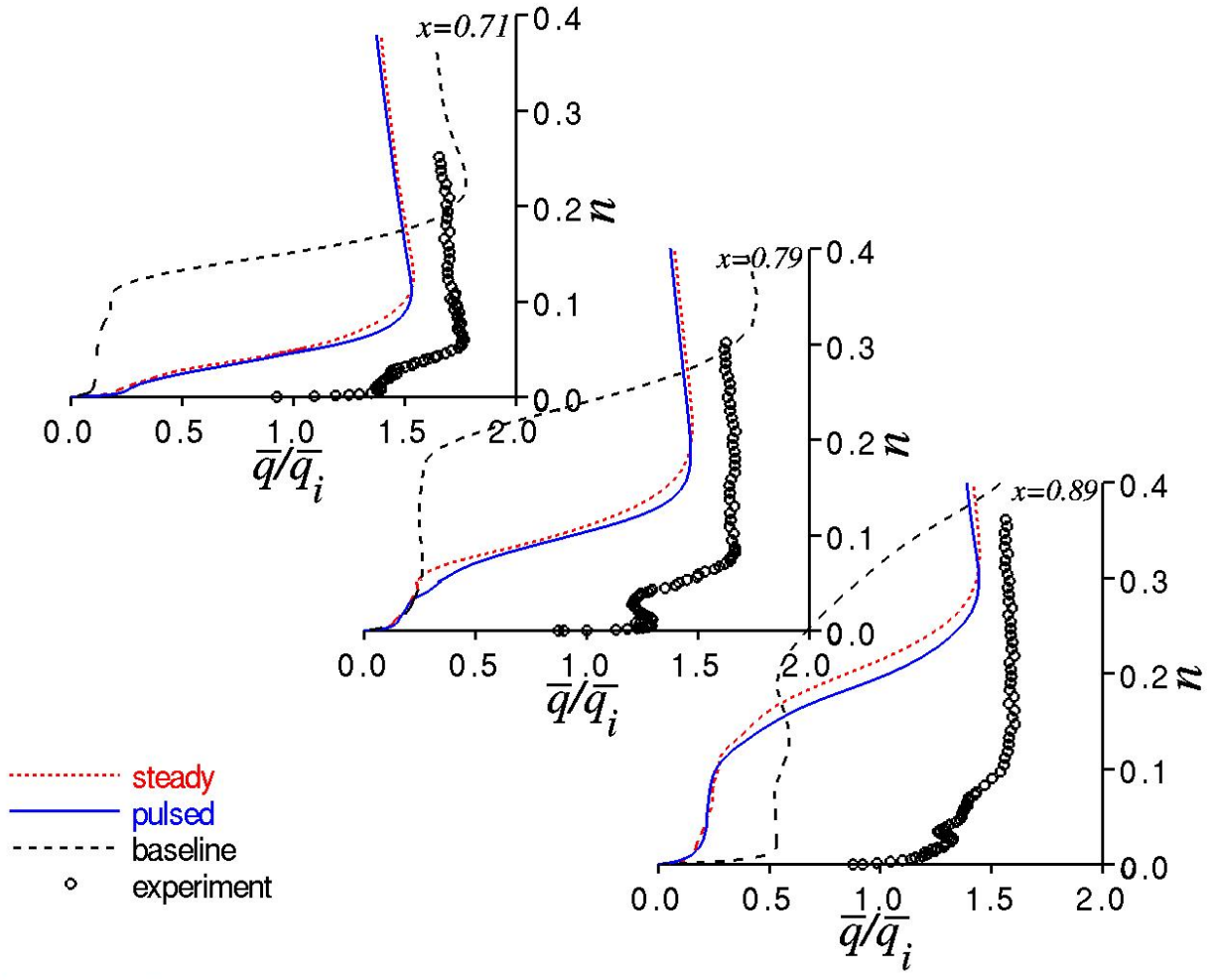


Figure 10: Time-mean velocity magnitude profiles at downstream stations.

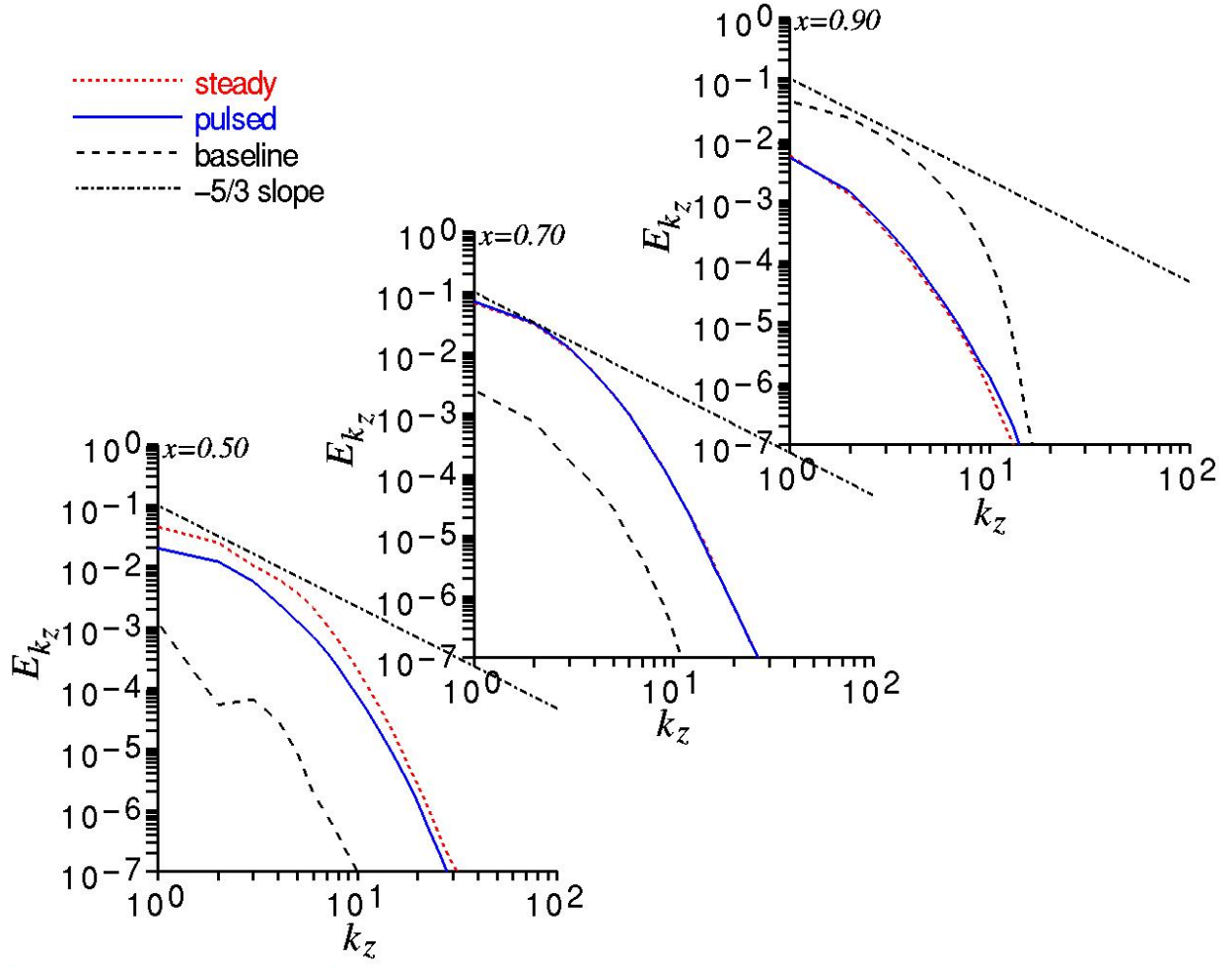


Figure 11: Time-mean turbulent kinetic energy spanwise wave-number spectra.

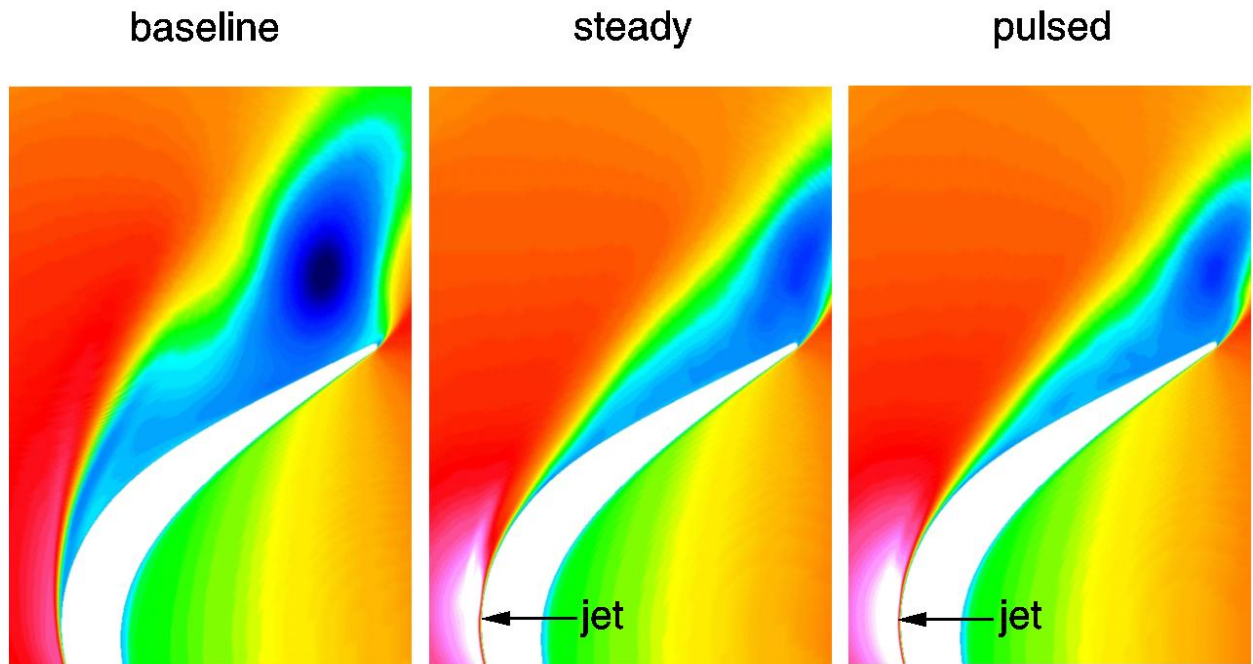


Figure 12: Time-mean planar contours of u velocity.

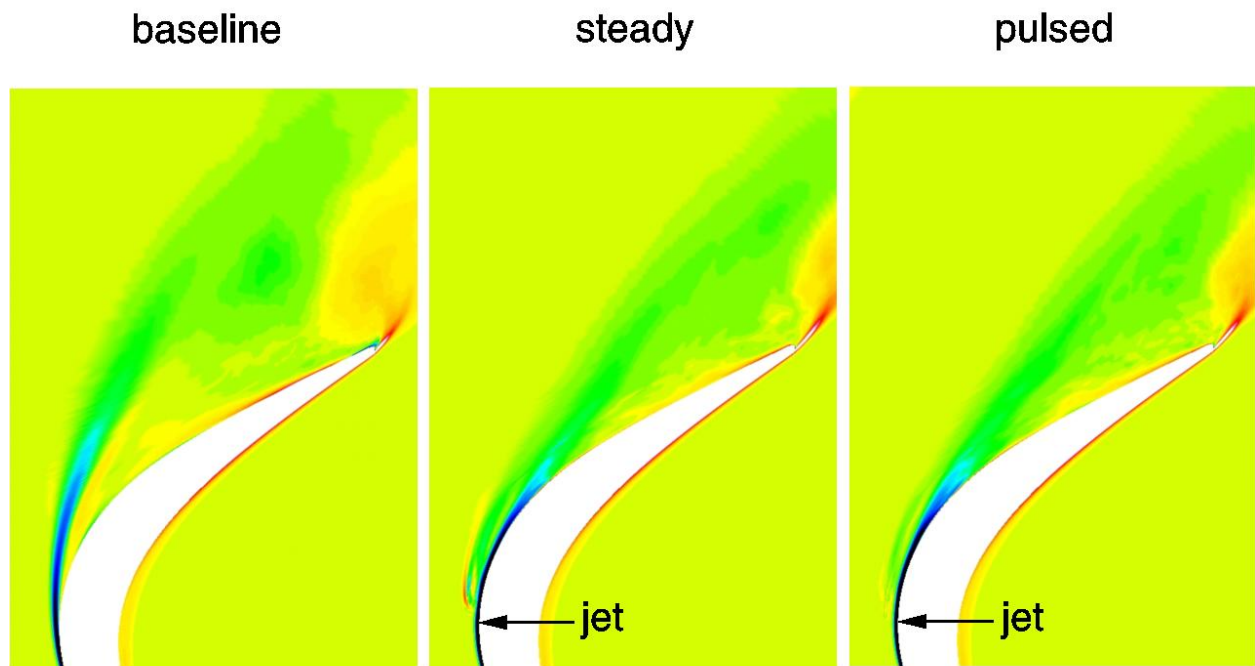


Figure 13: Time-mean contours of the spanwise component of vorticity.

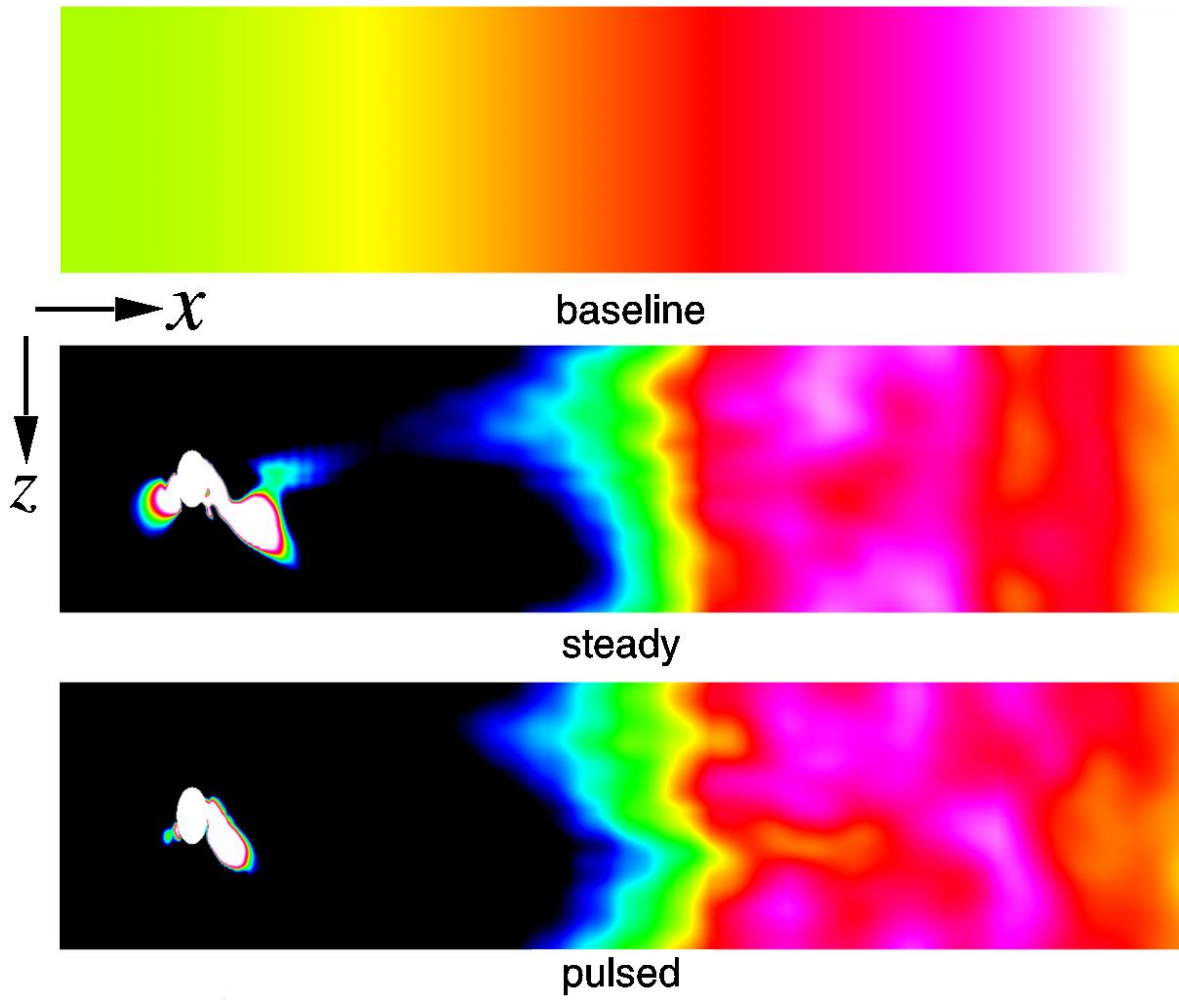


Figure 14: Time-mean contours of the spanwise component of vorticity on the blade surface.

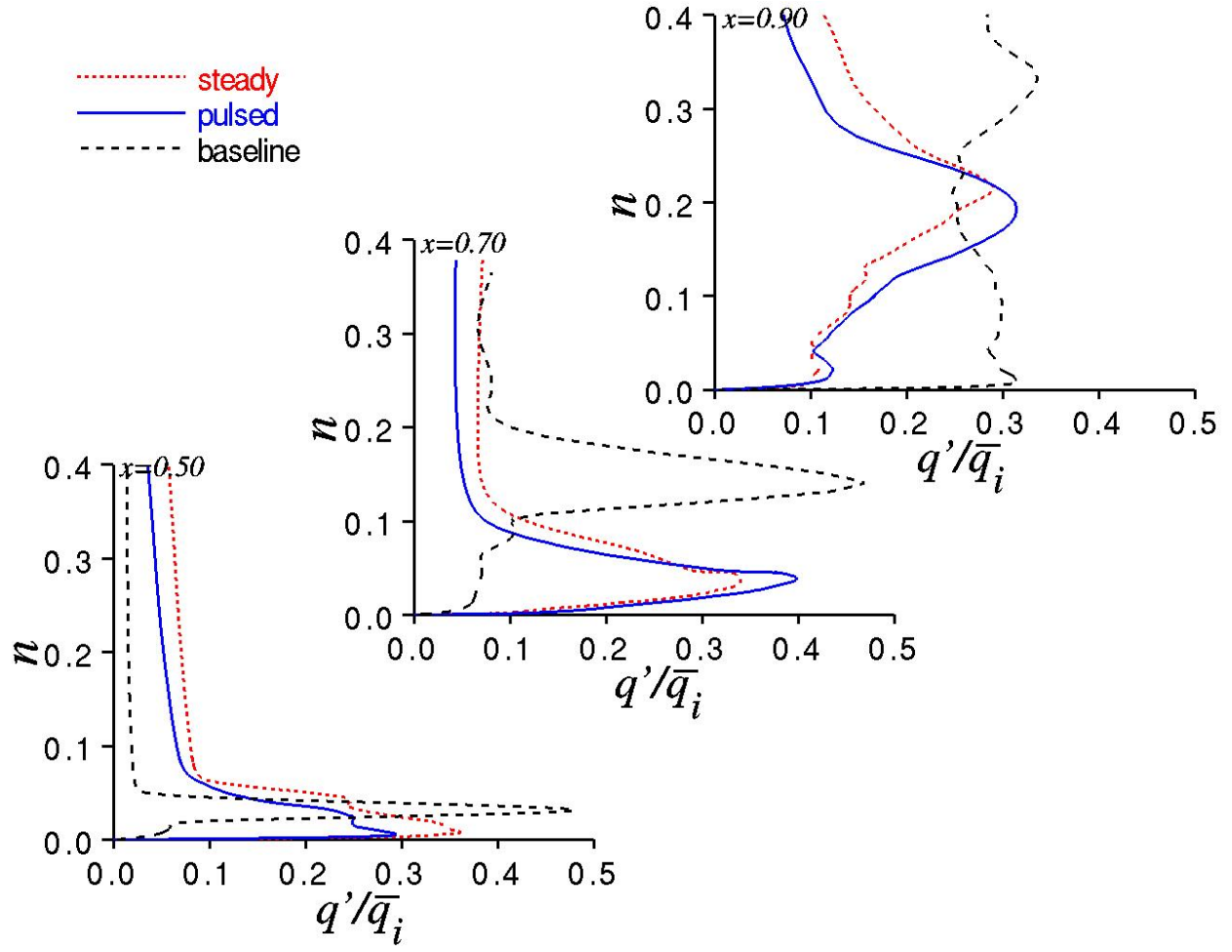


Figure 15: Time-mean fluctuating velocity magnitude profiles.

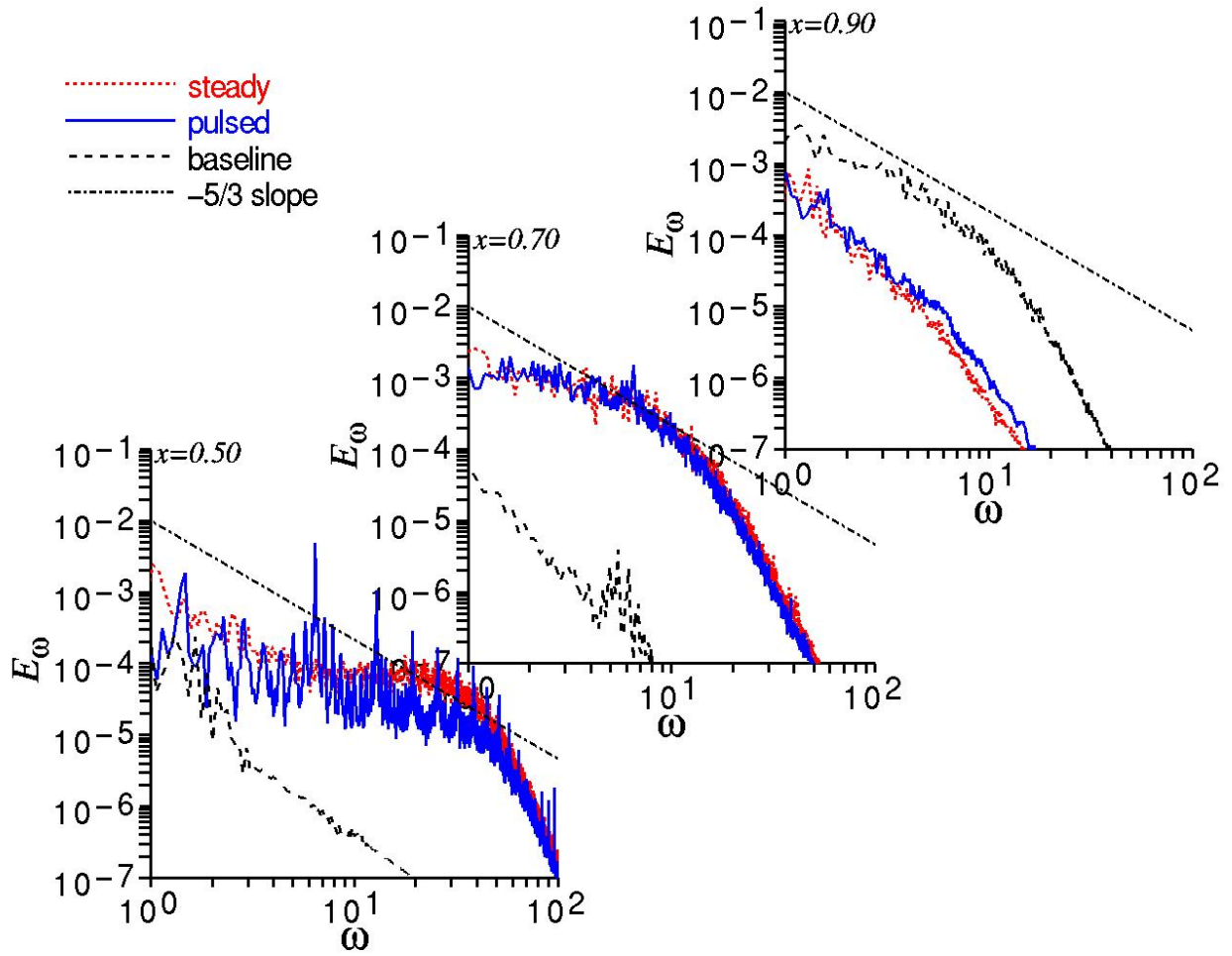


Figure 16: Turbulent kinetic energy frequency spectra.

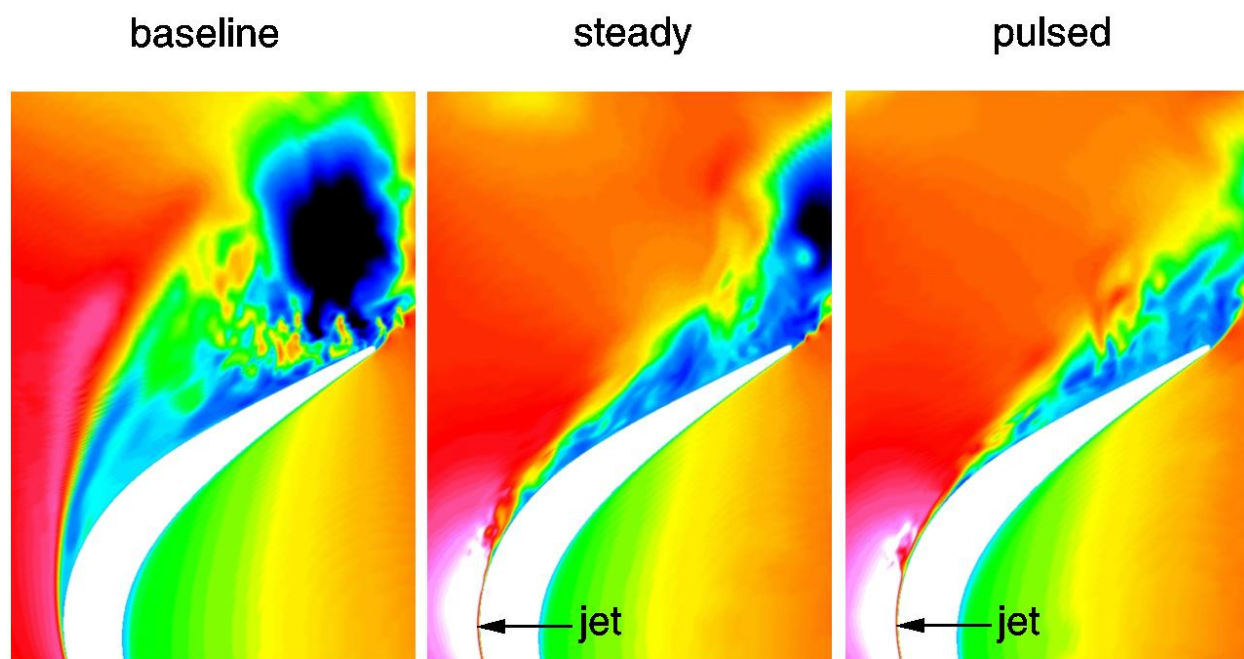


Figure 17: Instantaneous planar contours of u velocity.

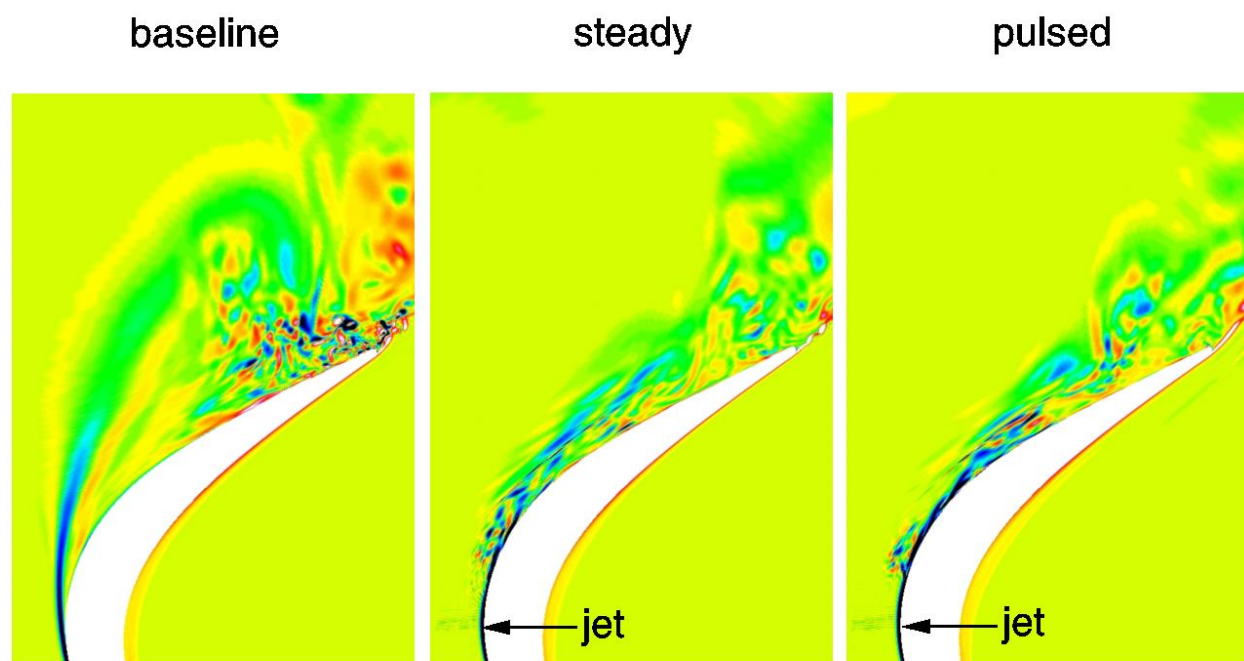


Figure 18: Instantaneous planar contours of the spanwise component of vorticity.

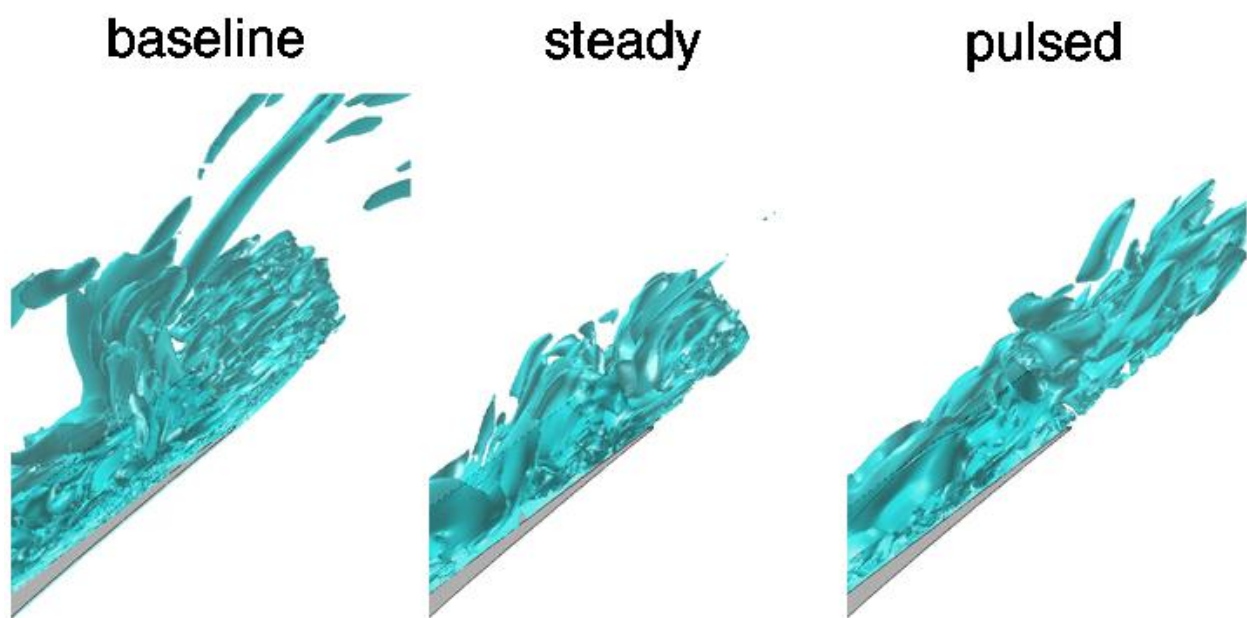


Figure 19: Instantaneous iso-surfaces of vorticity magnitude in the trailing-edge region.

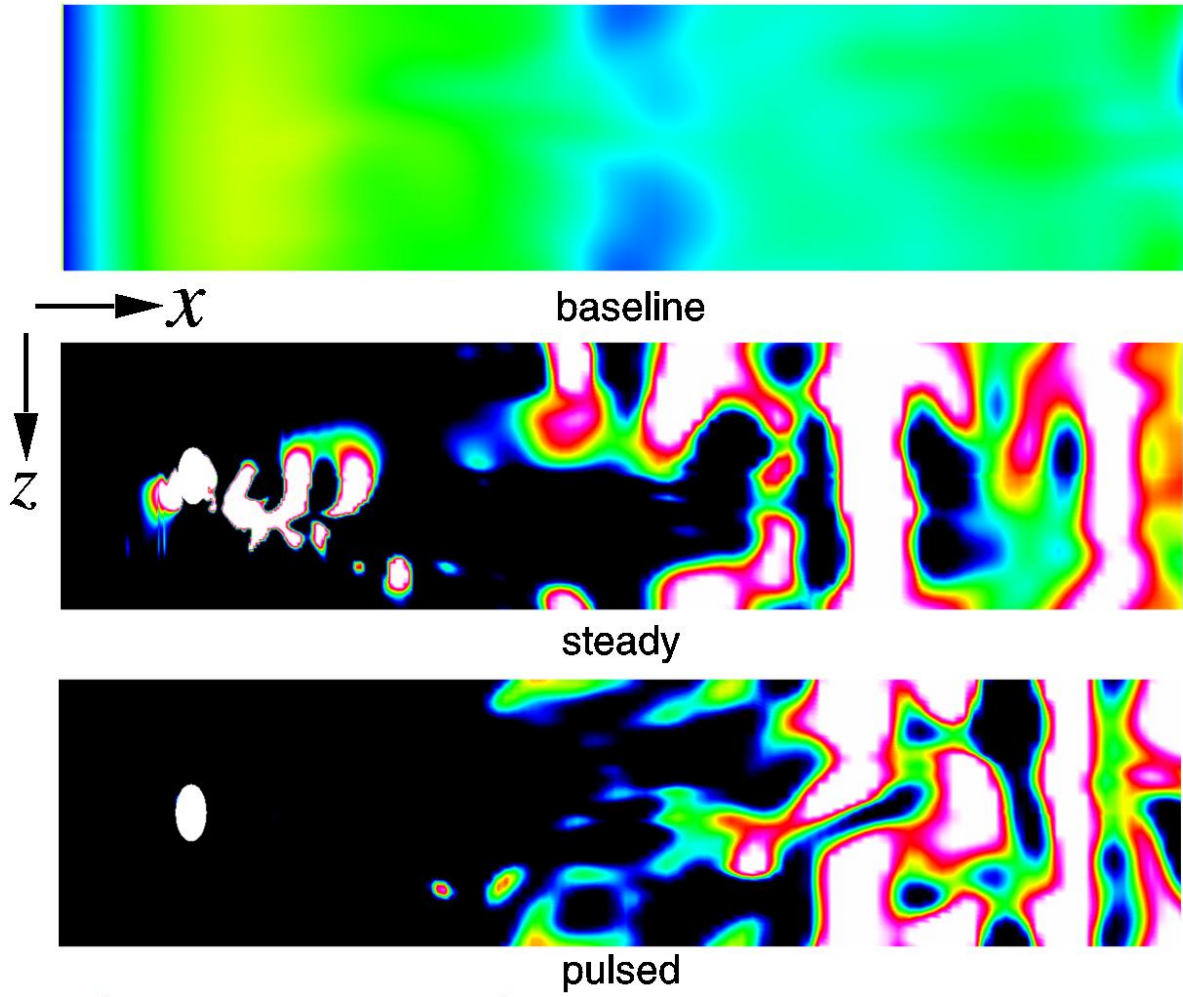


Figure 20: Instantaneous planar contours of the spanwise component of vorticity on the blade surface.

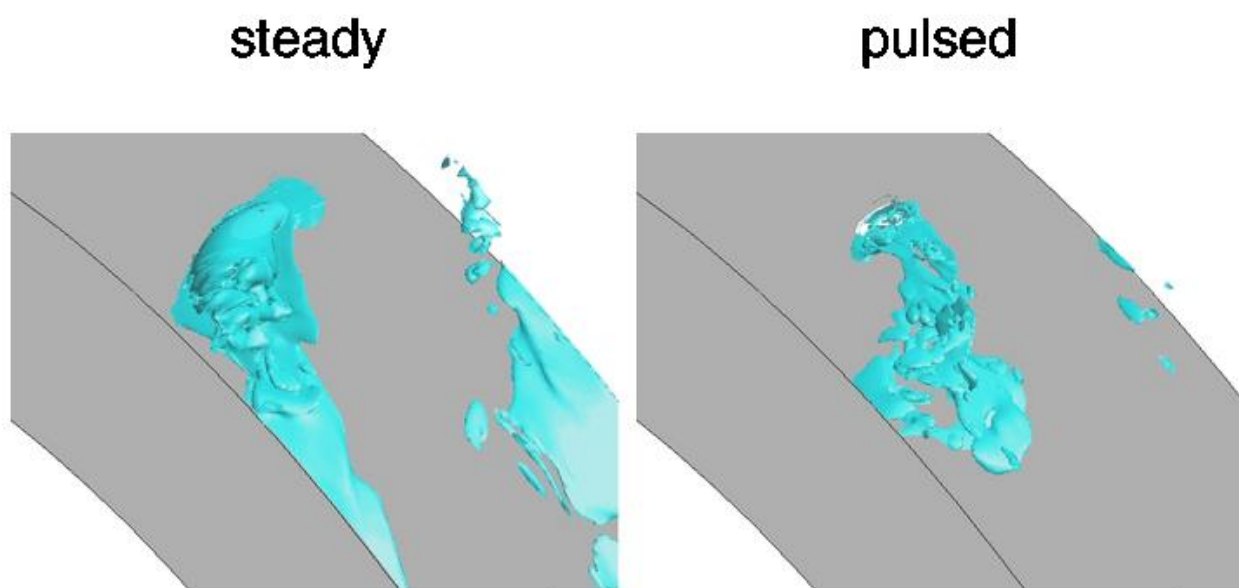


Figure 21: Instantaneous iso-surfaces of vorticity magnitude in the near-jet region.

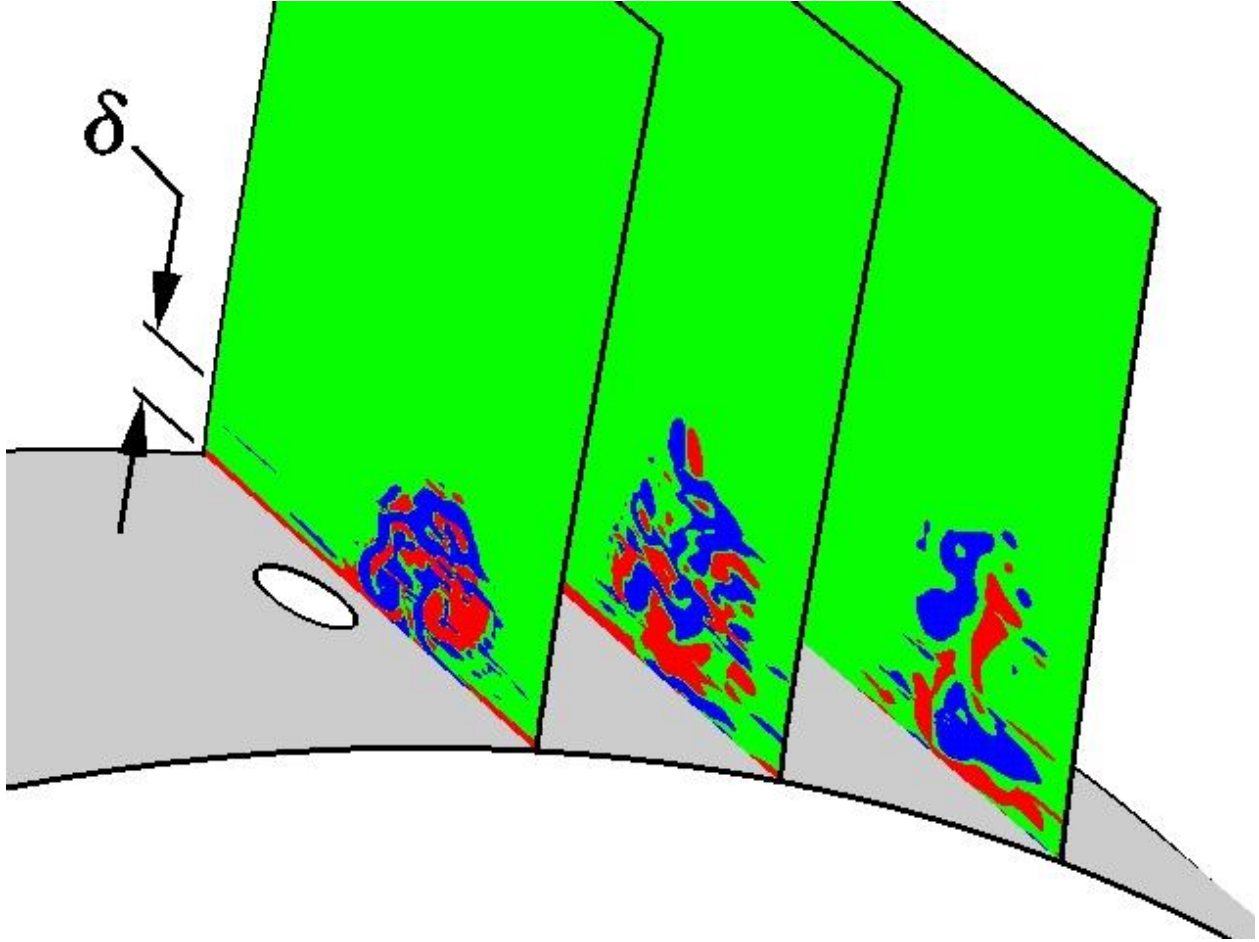


Figure 22: Instantaneous planar contours of the streamwise component of vorticity for the steady injection case.

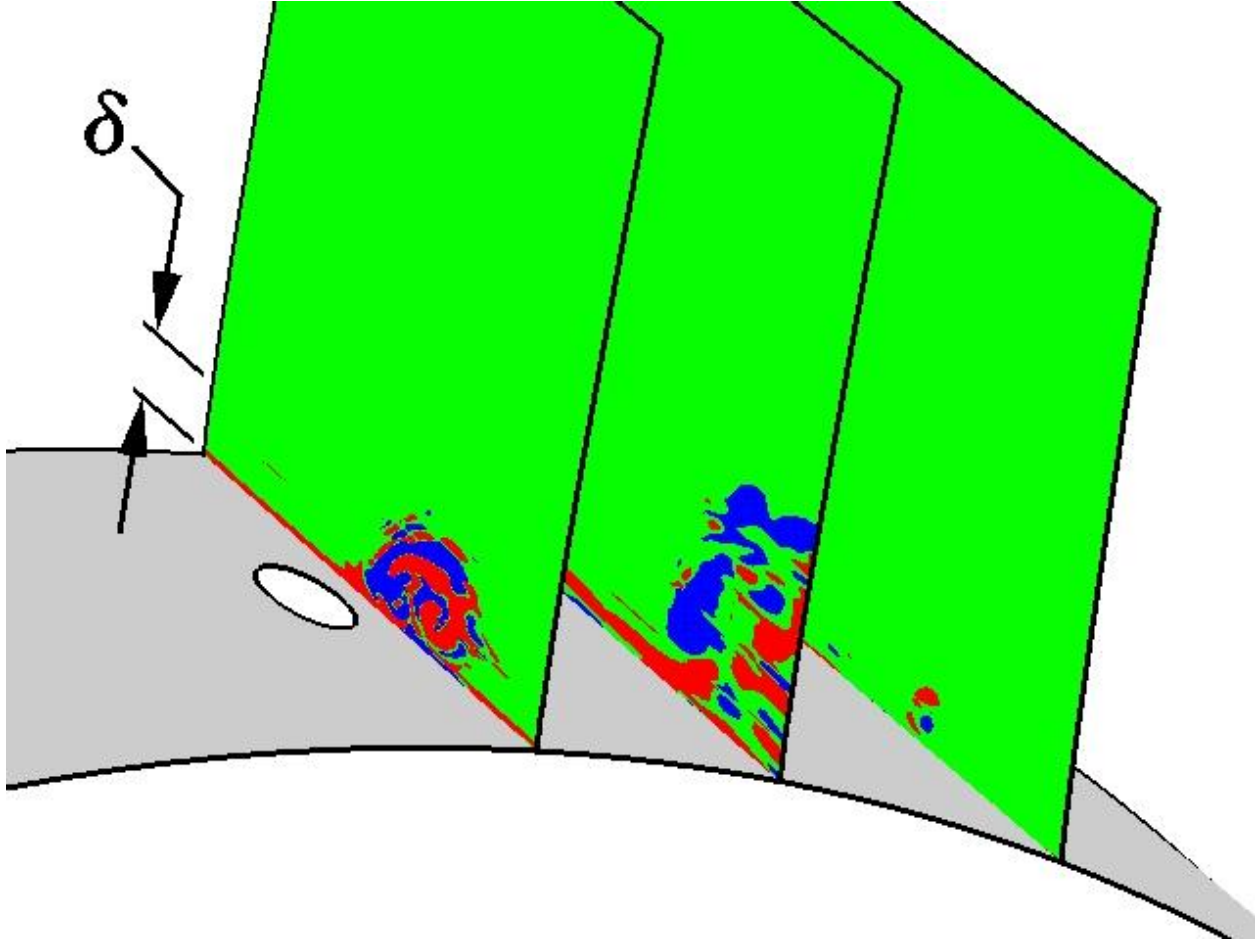


Figure 23: Instantaneous planar contours of the streamwise component of vorticity for the pulsed injection case at $t/t_p = 0.5$.

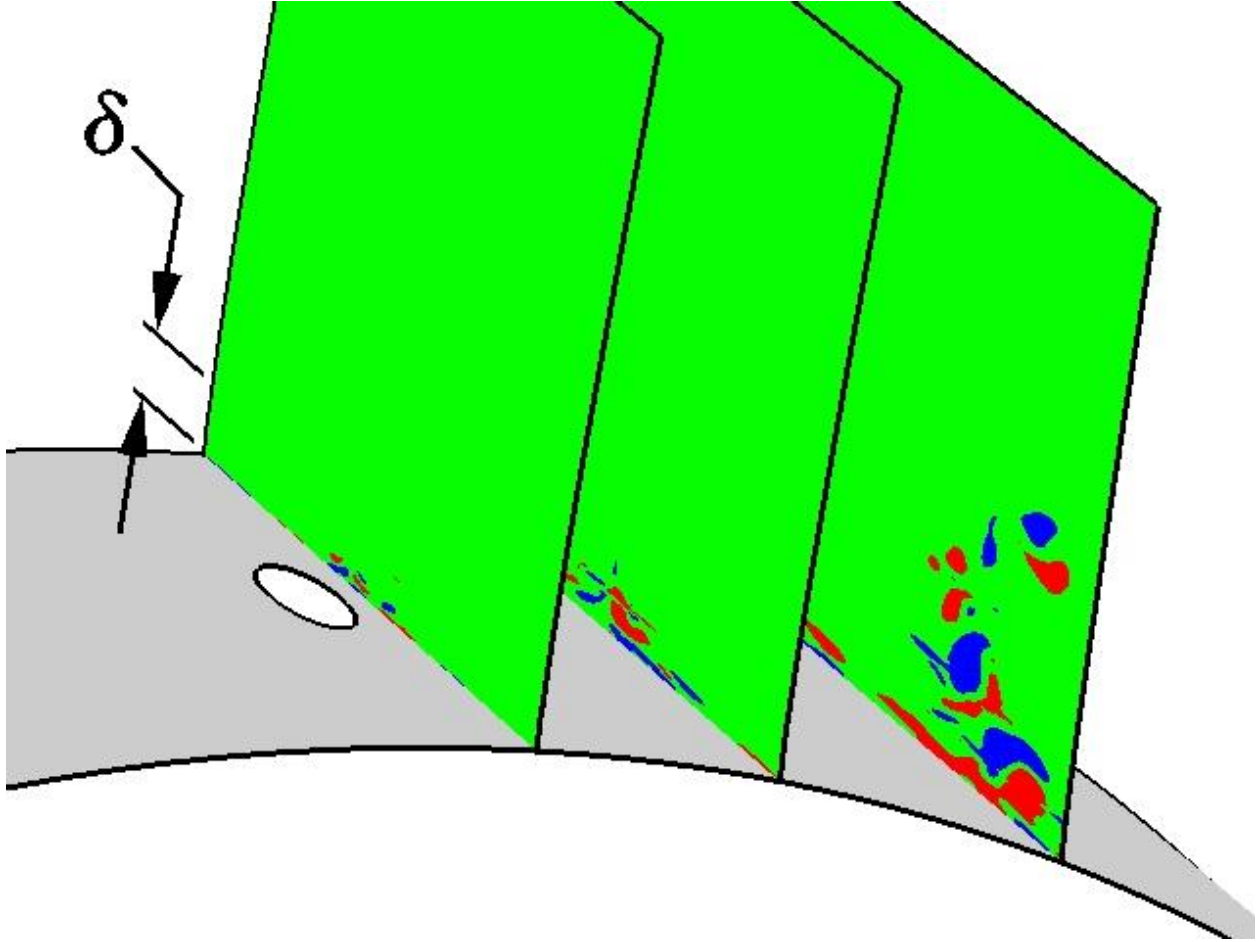


Figure 24: Instantaneous planar contours of the streamwise component of vorticity for the pulsed injection case at $t/t_p = 1.0$.

7. References

- [1] Halstead, D. E., Wisler, D. C., Okiishi, T. H., Walker, G. J., Hodson, H. P., and Shin, H. W., “Boundary Layer Development in Axial Compressors and Turbines Part 1 of 4: Composite Picture,” ASME Paper 95-GT-461, Jun. 1995.
- [2] Halstead, D. E., Wisler, D. C., Okiishi, T. H., Walker, G. J., Hodson, H. P., and Shin, H. W., “Boundary Layer Development in Axial Compressors and Turbines Part 3 of 4: LP Turbines,” ASME Paper 95-GT-463, Jun. 1995.
- [3] Simon, T. W. and Volino, R. J., “Separating and Separated Boundary Layers,” Technical Report WL-TR-96-2092, Wright Laboratory, Wright-Patterson AFB, OH, Feb. 1996.
- [4] Baughn, J. W., Butler, R. J., Byerley, A. R., and Rivir, R. B., “An Experimental Investigation of Heat Transfer, Transition and Separation on Turbine Blades at Low Reynolds Number and High Turbulence Intensity,” Technical Report WL-TR-96-2093, Wright Laboratory, Wright-Patterson AFB, OH, Jul. 1996.
- [5] Murawski, C. G., Simon, T. W., Volino, R. J., and Vafai, K., “Experimental Study of the Unsteady Aerodynamics in a Linear Cascade with Low Reynolds Number Low Pressure Turbine Blades,” ASME Paper 97-GT-95, Jun. 1997.
- [6] Qui, S. and Simon, T. W., “An Experimental Investigation of Transition as Applied to Low Pressure Turbine Suction Surface Flows,” ASME Paper 97-GT-455, Jun. 1997.
- [7] Welsh, S. T., Barlow, D. N., Butler, R. J., Van Treuren, K. W., Byerley, A. R., Baughn, J. W., and Rivir, R. B., “Effects of Passive and Active Air-Jet Turbulence on Turbine Blade Heat Transfer,” ASME Paper 97-GT-131, Jun. 1997.
- [8] Murawski, C. G. and Vafai, K., “Effect of Variable Axial Chord on a Low-Pressure Turbine Blade,” *Journal of Propulsion and Power*, Vol. 15, No. 5, Sep. 1999, pp. 667–674.
- [9] Lake, J. P., King, P. I., and Rivir, R. B., “Reduction of Separation Losses on a Turbine Blade With Low Reynolds Number,” AIAA Paper 99-0242, Jan. 1999.
- [10] Bons, J. P., Sondergaard, R., and Rivir, R. B., “Control of Low-Pressure Turbine Separation Using Vortex Generator Jets,” AIAA Paper 99-0367, Jan. 1999.
- [11] Bons, J. P., Sondergaard, R., and Rivir, R. B., “Turbine Separation Control Using Pulsed Vortex Generator Jets,” *Journal of Turbomachinery*, Vol. 123, No. 2, Apr. 2001, pp. 198–206.
- [12] Bons, J. P., Sondergaard, R., and Rivir, R. B., “The Fluid Dynamics of LPT Blade Separation Control Using Pulsed Jets,” *Journal of Turbomachinery*, Vol. 124, No. 1, Jan. 2002, pp. 77–85.
- [13] Sondergaard, R., Rivir, R. B., and Bons, J. P., “Control of Low-Pressure Turbine Separation Using Vortex Generator Jets,” *Journal of Propulsion and Power*, Vol. 18, No. 4, Jul.-Aug. 2002, pp. 889–895.
- [14] Huang, J., Corke, T. C., and Thomas, F. O., “Plasma Actuators for Separation Control of Low Pressure Turbine Blades,” AIAA Paper 2003-1027, Jan. 2003.
- [15] Sondergaard, R., Bons, J. P., Sucher, M., and Rivir, R. B., “Reducing Low-Pressure Turbine Stage Blade Count Using Vortex Generator Jet Separation Control,” ASME Paper GT-2002-30602, Jun. 2002.
- [16] Eulitz, F. and Engel, K., “Numerical Investigation of Wake Interaction in a Low Pressure Turbine,” ASME Paper 98-GT-563, Jun. 1998.
- [17] Choi, C. H. and Yoo, J. Y., “Cascade Flow Calculations Using the $k - \omega$ Turbulence Model with Explicit-Implicit Solver,” *AIAA Journal*, Vol. 35, No. 9, Sep. 1998, pp. 1551–1552.

- [18] Chernobrovkin, A. and Lakshminarayana, B., "Turbulence Modeling and Computation of Viscous Transitional Flows for Low Pressure Turbines," *Journal of Fluids Engineering*, Vol. 121, No. 4, Dec. 1999, pp. 824–833.
- [19] Dorney, D. J., Ashpis, D. E., Halstead, D. E., and Wisler, D. C., "Study of Boundary-Layer Development in a Two-Stage Low-Pressure Turbine," *Journal of Propulsion and Power*, Vol. 16, No. 1, Jan.-Feb. 2000, pp. 160–163.
- [20] Suzen, Y. B., Huang, P. G., Hultgren, L. S., and Ashpis, D. E., "Predictions of Separated and Transitional Boundary Layers Under Low-Pressure Turbine Airfoil Conditions Using an Intermittency Transport Equation," AIAA Paper 2001-0446, Jan. 2001.
- [21] Raverdy, B., Mary, I., Sagaut, P., and Liams, N., "Large-Eddy Simulation of the Flow Around a Low Pressure Turbine Blade," *Direct and Large-Eddy Simulation IV, ERCOFTAC Series Vol. 8*, edited by B. J. Guerts, R. Friedrich, and O. Metais, Kluwer Academic Publishers, Dordrecht, The Netherlands, 2001, pp. 381–388.
- [22] Mittal, R., Venkatasubramanian, S., and Najjar, F. M., "Large-Eddy Simulation of Flow Through a Low-Pressure Turbine Cascade," AIAA Paper 2001-2560, Jun. 2001.
- [23] Postl, D., Gross, A., and Fasel, H. F., "Numerical Investigation of Low-Pressure Turbine Blade Separation Control," AIAA Paper 2003-0614, Jan. 2003.
- [24] Rizzetta, D. P. and Visbal, M. R., "Numerical Investigation of Transitional Flow Through a Low-Pressure Turbine Cascade," AIAA Paper 2003-3587, Jun. 2003.
- [25] Wissink, J. G., "DNS of Separating, Low-Reynolds Number Flow in a Turbine Cascade with Incoming Wakes," *International Journal of Heat and Fluid Flow*, Vol. 24, No. 4, Aug. 2003, pp. 626–635.
- [26] Kalitzin, G., Wu, X., and Durbin, P. A., "DNS of Fully Turbulent Flow in a LPT Passage," *International Journal of Heat and Fluid Flow*, Vol. 24, No. 4, Aug. 2003, pp. 636–644.
- [27] Rizzetta, D. P. and Visbal, M. R., "Numerical Simulation of Separation Control for a Highly-Loaded Low-Pressure Turbine," AIAA Paper 2004-2204, Jun.-Jul. 2004.
- [28] Gross, A. and Fasel, H. F., "Active Control of Separation for Low-Pressure Turbine Blades," AIAA Paper 2004-2203, Jun.-Jul. 2004.
- [29] Rivir, R. B., Sondergaard, R., Bons, J. P., and Yurchenko, N., "Control of Separation in Turbine Boundary Layers," AIAA Paper 2004-2201, Jun.-Jul. 2004.
- [30] Beam, R. and Warming, R., "An Implicit Factored Scheme for the Compressible Navier-Stokes Equations," *AIAA Journal*, Vol. 16, No. 4, Apr. 1978, pp. 393–402.
- [31] Gordnier, R. E. and Visbal, M. R., "Numerical Simulation of Delta-Wing Roll," AIAA Paper 93-0554, Jan. 1993.
- [32] Jameson, A., Schmidt, W., and Turkel, E., "Numerical Solutions of the Euler Equations by Finite Volume Methods Using Runge-Kutta Time Stepping Schemes," AIAA Paper 81-1259, Jun. 1981.
- [33] Pulliam, T. H. and Chaussee, D. S., "A Diagonal Form of an Implicit Approximate-Factorization Algorithm," *Journal of Computational Physics*, Vol. 39, No. 2, Feb. 1981, pp. 347–363.
- [34] Lele, S. A., "Compact Finite Difference Schemes with Spectral-like Resolution," *Journal of Computational Physics*, Vol. 103, No. 1, Nov. 1992, pp. 16–42.
- [35] Visbal, M. R. and Gaitonde, D. V., "High-Order-Accurate Methods for Complex Unsteady Subsonic Flows," *AIAA Journal*, Vol. 37, No. 10, Oct. 1999, pp. 1231–1239.
- [36] Gaitonde, D., Shang, J. S., and Young, J. L., "Practical Aspects of High-Order Accurate Finite-Volume Schemes for Electromagnetics," AIAA Paper 97-0363, Jan. 1997.

- [37] Gaitonde, D. and Visbal, M. R., “High-Order Schemes for Navier-Stokes Equations: Algorithm and Implementation into FDL3DI,” Technical Report AFRL-VA-WP-TR-1998-3060, Air Force Research Laboratory, Wright-Patterson AFB, OH, Aug. 1998.
- [38] Gordnier, R. E. and Visbal, M. R., “Numerical Simulation of Delta-Wing Roll,” *Aerospace Science and Technology*, Vol. 2, No. 6, Sep. 1998, pp. 347–357.
- [39] Gordnier, R. E., “Computation of Delta-Wing Roll Maneuvers,” *Journal of Aircraft*, Vol. 32, No. 3, May 1995, pp. 486–492.
- [40] Visbal, M. R., “Computational Study of Vortex Breakdown on a Pitching Delta Wing,” AIAA Paper 93-2974, Jul. 1993.
- [41] Visbal, M., Gaitonde, D., and Gogineni, S., “Direct Numerical Simulation of a Forced Transitional Plane Wall Jet,” AIAA Paper 98-2643, Jun. 1998.
- [42] Rizzetta, D. P., Visbal, M. R., and Stanek, M. J., “Numerical Investigation of Synthetic-Jet Flowfields,” *AIAA Journal*, Vol. 37, No. 8, Aug. 1999, pp. 919–927.
- [43] Rizzetta, D. P., Visbal, M. R., and Blaisdell, G. A., “A Time-Implicit High-Order Compact Differencing and Filtering Scheme for Large-Eddy Simulation,” *International Journal for Numerical Methods in Fluids*, Vol. 42, No. 6, Jun. 2003, pp. 665–693.
- [44] Rizzetta, D. P. and Visbal, M. R., “Application of Large-Eddy Simulation to Supersonic Compression Ramps,” *AIAA Journal*, Vol. 40, No. 8, Aug. 2002, pp. 1574–1581.
- [45] Rizzetta, D. P., Visbal, M. R., and Gaitonde, D. V., “Large-Eddy Simulation of Supersonic Compression-Ramp Flow by a High-Order Method,” *AIAA Journal*, Vol. 39, No. 12, Dec. 2001, pp. 2283–2292.
- [46] Rizzetta, D. P. and Visbal, M. R., “Large-Eddy Simulation of Supersonic Cavity Flowfields Including Flow Control,” *AIAA Journal*, Vol. 41, No. 8, Aug. 2003, pp. 1452–1462.
- [47] Steinbrenner, J. P., Chawner, J. P., and Fouts, C. L., “The GRIDGEN 3D Multiple Block Grid Generation System, Volume II: User’s Manual,” Technical Report WRDC-TR-90-3022, Wright Research and Development Center, Wright-Patterson AFB, OH, Feb. 1991.
- [48] Gruber, B. and Carstens, V., “The Impact of Viscous Effects on the Aerodynamic Damping of Vibrating Transonic Compressor Blades-A Numerical Study,” *Journal of Turbomachinery*, Vol. 123, No. 2, Apr. 2001, pp. 409–417.
- [49] Visbal, M. R. and Gaitonde, D. V., “Very High-Order Spatially Implicit Schemes for Computational Acoustics on Curvilinear Meshes,” *Journal of Computational Acoustics*, Vol. 9, No. 4, Dec. 2001, pp. 1259–1286.
- [50] Sherer, S. E., “Further Analysis of High-Order Overset Grid Method with Applications,” AIAA Paper 2003-3839, Jun. 2003.
- [51] Suhs, N. E., Rogers, S. E., and Dietz, W. E., “PEGASUS 5: An Automated Preprocessor for Overset-Grid Computational Fluid Dynamics,” *AIAA Journal*, Vol. 41, No. 6, Jun. 2003, pp. 1037–1045.
- [52] Message Passing Interface Forum, “MPI: A Message-Passing Interface Standard,” Computer Science Department Technical Report CS-94-230, University of Tennessee, Knoxville, TN, Apr. 1994.

List of Symbols

C_p	= turbine blade time-mean surface pressure coefficient, $2(\bar{p} - \bar{p}_i)/\rho_i \bar{q}_i^2$
\mathcal{D}	= duty cycle expressed as a decimal fraction
E_{kz}, E_ω	= nondimensional turbulent kinetic energy wave number and frequency spectra
f	= dimensional jet forcing frequency
\mathcal{J}	= Jacobian of the coordinate transformation
k_z	= nondimensional spanwise wave number
l, n	= nondimensional blade tangential and normal directions
M	= Mach number
p	= nondimensional static pressure
Pr	= Prandtl number, 0.73 for air
q	= nondimensional planar velocity magnitude, $\sqrt{u^2 + v^2}$ or $\sqrt{v^2 + w^2}$ for the jet
Re_∞	= reference Reynolds number, $\rho_\infty q_\infty c/\mu_\infty$
Re	= chord inlet Reynolds number, $\rho_i \bar{q}_i Re_\infty/\mu_i$
t	= nondimensional time based upon the reference velocity, u_∞
t_p	= nondimensional jet forcing period
T	= nondimensional static temperature
in the x, y, z directions	
u_1, u_2, u_3	= u, v, w
U, V, W	= contravariant velocity components
x, y, z	= nondimensional Cartesian coordinates in the streamwise, vertical, and spanwise directions
x_1, x_2, x_3	= x, y, z
α	= turbine blade flow angle
γ	= specific heat ratio, 1.4 for air
δ	= nondimensional boundary-layer thickness
δ_{ij}	= Kronecker delta function
$\delta_{\xi 2}, \delta_{\eta 2}, \delta_{\zeta 2},$ $\delta_{\xi 4}, \delta_{\eta 4}, \delta_{\zeta 4}$	= 2nd-order and 4th-order finite-difference operators in ξ, η, ζ
$\Delta l, \Delta n, \Delta z$	= nondimensional mesh step sizes in blade tangential, normal, and spanwise directions
μ	= nondimensional molecular viscosity coefficient
$\xi_t, \xi_x, \xi_y, \xi_z,$ $\eta_t, \eta_x, \eta_y, \eta_z,$ $\zeta_t, \zeta_x, \zeta_y, \zeta_z$	= metric coefficients of the coordinate transformation
ω	= nondimensional frequency
<i>Subscripts</i>	
i, o	= inflow and outflow conditions
j	= corresponding to vortex generator jet
max, min	= maximum and minimum values
l	= “local freestream value”
∞	= dimensional reference value
<i>Superscripts</i>	
+	= value given in law-of-the-wall units
—	= time-mean quantity
'	= root-mean-square fluctuating component